2-11-2014

First Searches for Optical Counterparts to Gravitational-Wave Candidate Events

Tiffany Summerscales
Andrews University, tzs@andrews.edu

LIGO Scientific Collaboration and Virgo Collaboration

The Astrophysical Journal Supplement Series, 211:7 (25pp), 2014 March doi:10.1088/0067-0049/211/1/7

FIRST SEARCHES FOR OPTICAL COUNTERPARTS TO GRAVITATIONAL-WAVE CANDIDATE EVENTS

J. Aasi[1], J. Abadie[1], B. P. Abbott[1], R. Abbott[1], T. Abbott[2], M. R. Abernathy[1], T. Accadia[3], F. Acernese[4,5], C. Adams[6], T. Adams[7], R. X. Adhikari[1], C. Affeldt[8], M. Agathos[9], N. Aggarwal[10], O. D. Aguiar[11], P. Ajith[1], B. Allen[8,12,13], A. Allocca[14,15], E. Amador Ceron[12], D. Amariutei[16], R. A. Anderson[1], S. B. Anderson[1], W. G. Anderson[12], K. Arai[1], M. C. Araya[1], C. Arceneaux[17], J. Areeda[18], S. Ast[13], S. M. Aston[6], P. Astone[19], P. Aufmuth[13], C. Aulbert[8], L. Austin[1], B. E. Aylott[20], S. Babak[21], P. T. Baker[22], G. Ballardin[23], S. W. Ballmer[24], J. C. Barayoga[1], D. Barker[25], S. H. Barnum[10], F. Barone[4,5], B. Barr[26], L. Barsotti[10], M. Barsuglia[27], M. A. Barton[25], I. Bartos[28], R. Bassiri[26,29], A. Basti[14,30], J. Batch[25], J. Bauchrowitz[8], Th. S. Bauer[9], M. Bebronne[3], B. Behnke[21], M. Bejger[31], M. G. Beker[9], A. S. Bell[26], C. Bell[26], I. Belopolski[28], G. Bergmann[8], J. M. Berliner[25], A. Bertolini[9], D. Bessis[32], J. Betzwieser[6], P. T. Beyersdorf[33], T. Bhadbhade[29], I. A. Bilenko[34], G. Billingsley[1], J. Birch[6], M. Bitossi[14], M. A. Bizouard[35], E. Black[1], J. K. Blackburn[1], L. Blackburn[36], D. Blair[37], M. Blom[9], O. Bock[8], T. P. Bodiya[10], M. Boer[38,39], C. Bogan[8], C. Bond[20], F. Bondu[40], L. Bonelli[14,30], R. Bonnand[41], R. Bork[1], M. Born[8], S. Bose[42], L. Bosi[43], J. Bowers[2], C. Bradaschia[14], P. R. Brady[12], V. B. Braginsky[34], M. Branchesi[44,45], C. A. Brannen[42], J. E. Brau[46], J. Breyer[8], T. Briant[47], D. O. Bridges[6], A. Brillet[38], M. Brinkmann[8], V. Brisson[35], M. Britzger[8], A. F. Brooks[1], D. A. Brown[24], D. D. Brown[20], F. Brückner[20], T. Bulik[48], H. J. Bulten[9,49], A. Buonanno[50], D. Buskulic[3], C. Buy[27], R. L. Byer[29], L. Cadonati[51], G. Cagnoli[41], J. Calderón Bustillo[52], E. Calloni[4,53], J. B. Camp[36], P. Campsie[26], K. C. Cannon[54], B. Canuel[23], J. Cao[55], C. D. Capano[50], F. Carbognani[23], L. Carbone[20], S. Caride[56], A. Castiglia[57], S. Caudill[12], M. Cavaglià[17], F. Cavalier[35], R. Cavalieri[23], G. Cella[14], C. Cepeda[1], E. Cesarini[58], R. Chakraborty[1], T. Chalermsongsak[1], S. Chao[59], P. Charlton[60], E. Chassande-Mottin[27], X. Chen[37], Y. Chen[61], A. Chincarini[62], A. Chiummo[23], H. S. Cho[63], J. Chow[64], N. Christensen[65], Q. Chu[37], S. S. Y. Chua[64], S. Chung[37], G. Ciani[16], F. Clara[25], D. E. Clark[29], J. A. Clark[51], F. Cleva[38], E. Coccia[58,66], P.-F. Cohadon[47], A. Colla[19,67], M. Colombini[43], M. Constancio, Jr.[11], A. Conte[19,67], R. Conte[68,69], D. Cook[25], T. R. Corbitt[2], M. Cordier[33], N. Cornish[22], A. Corsi[70], C. A. Costa[11], M. W. Coughlin[71], J.-P. Coulon[38], S. Countryman[28], P. Couvares[24], D. M. Coward[37], M. Cowart[6], D. C. Coyne[1], K. Craig[26], J. D. E. Creighton[12], T. D. Creighton[32], S. G. Crowder[72], A. Cumming[26], L. Cunningham[26], E. Cuoco[23], K. Dahl[8], T. Dal Canton[8], M. Damjanic[8], S. L. Danilishin[37], S. D'Antonio[58], K. Danzmann[8,13], V. Dattilo[23], B. Daudert[1], H. Daveloza[32], M. Davier[35], G. S. Davies[26], E. J. Daw[73], R. Day[23], T. Dayanga[42], R. De Rosa[4,53], G. Debreczeni[74], J. Degallaix[41], W. Del Pozzo[9], E. Deleeuw[16], S. Deléglise[47], T. Denker[8], H. Dereli[38], V. Dergachev[1], R. DeRosa[2], R. DeSalvo[68,69], S. Dhurandhar[75], L. Di Fiore[4], A. Di Lieto[14,30], I. Di Palma[8], A. Di Virgilio[14], M. Díaz[32], A. Dietz[17], K. Dmitry[34], F. Donovan[10], K. L. Dooley[8], S. Doravari[6], M. Drago[76,77], R. W. P. Drever[78], J. C. Driggers[1], Z. Du[55], J.-C. Dumas[37], S. Dwyer[25], T. Eberle[8], M. Edwards[7], A. Effler[2], P. Ehrens[1], J. Eichholz[16], S. S. Eikenberry[16], G. Endrőczi[74], R. Essick[10], T. Etzel[1], K. Evans[26], M. Evans[10], T. Evans[6], M. Factourovich[28], V. Fafone[58,66], S. Fairhurst[7], Q. Fang[37], B. Farr[79], W. Farr[79], M. Favata[80], D. Fazi[79], H. Fehrmann[8], D. Feldbaum[6,16], I. Ferrante[14,30], F. Ferrini[23], F. Fidecaro[14,30], L. S. Finn[81], I. Fiori[23], R. Fisher[24], R. Flaminio[41], E. Foley[18], S. Foley[10], E. Forsi[6], L. A. Forte[4], N. Fotopoulos[1], J.-D. Fournier[38], S. Franco[35], S. Frasca[19,67], F. Frasconi[14], M. Frede[8], M. Frei[57], Z. Frei[82], A. Freise[20], R. Frey[46], T. T. Fricke[8], P. Fritschel[10], V. V. Frolov[6], M.-K. Fujimoto[83], P. Fulda[16], M. Fyffe[6], J. Gair[71], L. Gammaitoni[43,84], J. Garcia[25], F. Garufi[4,53], N. Gehrels[36], G. Gemme[62], E. Genin[23], A. Gennai[14], L. Gergely[82], S. Ghosh[42], J. A. Giaime[2,6], S. Giampanis[12], K. D. Giardina[6], A. Giazotto[14], S. Gil-Casanova[52], C. Gill[26], J. Gleason[16], E. Goetz[8], R. Goetz[16], L. Gondan[82], G. González[2], N. Gordon[26], M. L. Gorodetsky[34], S. Gossan[61], S. Goßler[8], R. Gouaty[3], C. Graef[8], P. B. Graff[36], M. Granata[41], A. Grant[26], S. Gras[10], C. Gray[25], R. J. S. Greenhalgh[85], A. M. Gretarsson[86], C. Griffo[18], H. Grote[8], K. Grover[20], S. Grunewald[21], G. M. Guidi[44,45], C. Guido[6], K. E. Gushwa[1], E. K. Gustafson[1], R. Gustafson[56], B. Hall[42], E. Hall[1], D. Hammer[12], G. Hammond[26], M. Hanke[8], J. Hanks[25], C. Hanna[87], J. Hanson[6], J. Harms[1], G. M. Harry[88], I. W. Harry[24], E. D. Harstad[46], M. T. Hartman[16], K. Haughian[26], K. Hayama[83], J. Heefner[1,144], A. Heidmann[47], M. Heintze[6,16], H. Heitmann[38], P. Hello[35], G. Hemming[23], M. Hendry[26], I. S. Heng[26], A. W. Heptonstall[1], M. Heurs[8], S. Hild[26], D. Hoak[51], K. A. Hodge[1], K. Holt[6], M. Holtrop[89], T. Hong[61], S. Hooper[37], T. Horrom[90], D. J. Hosken[91], J. Hough[26], E. J. Howell[37], Y. Hu[26], Z. Hua[55], V. Huang[59], E. A. Huerta[24], B. Hughey[86], S. Husa[52], S. H. Huttner[26], M. Huynh[12], T. Huynh-Dinh[6], J. Iafrate[2], D. R. Ingram[25], R. Inta[64], T. Isogai[10], A. Ivanov[1], B. R. Iyer[92], K. Izumi[25], M. Jacobson[1], E. James[1], H. Jang[93], Y. J. Jang[79], P. Jaranowski[94], F. Jiménez-Forteza[52], W. W. Johnson[2], D. Jones[25], D. I. Jones[95], R. Jones[26], R. J. G. Jonker[9], L. Ju[37], Haris K[96], P. Kalmus[1], V. Kalogera[79], S. Kandhasamy[72], G. Kang[93], J. B. Kanner[36], M. Kasprzack[23,35], R. Kasturi[97], E. Katsavounidis[10], W. Katzman[6], H. Kaufer[13], K. Kaufman[61], K. Kawabe[25], S. Kawamura[83], F. Kawazoe[8], F. Kéfélian[38], D. Keitel[8], D. B. Kelley[24], W. Kells[1], D. G. Keppel[8], A. Khalaidovski[8], F. Y. Khalili[34], E. A. Khazanov[98], B. K. Kim[93], C. Kim[93,99], K. Kim[100], N. Kim[29], W. Kim[91], Y.-M. Kim[63], E. J. King[91], P. J. King[1], D. L. Kinzel[6], J. S. Kissel[10], S. Klimenko[16], J. Kline[12], S. Koehlenbeck[8], K. Kokeyama[2], V. Kondrashov[1], S. Koranda[12], W. Z. Korth[1], I. Kowalska[48], D. Kozak[1], A. Kremin[72], V. Kringel[8], B. Krishnan[8], A. Królak[101,102], C. Kucharczyk[29], S. Kudla[2], G. Kuehn[8], A. Kumar[103], P. Kumar[24], R. Kumar[26], R. Kurdyumov[29], P. Kwee[10], M. Landry[25], B. Lantz[29], S. Larson[104], P. D. Lasky[105], C. Lawrie[26], A. Lazzarini[1],

A. Le Roux[6], P. Leaci[21], E. O. Lebigot[55], C.-H. Lee[63], H. K. Lee[100], H. M. Lee[99], J. Lee[10], J. Lee[18], M. Leonardi[76,77], J. R. Leong[8], N. Leroy[35], N. Letendre[3], B. Levine[25], J. B. Lewis[1], V. Lhuillier[25], T. G. F. Li[9], A. C. Lin[29], T. B. Littenberg[79], V. Litvine[1], F. Liu[106], H. Liu[7], Y. Liu[55], Z. Liu[16], D. Lloyd[1], N. A. Lockerbie[107], V. Lockett[18], D. Lodhia[20], K. Loew[86], J. Logue[26], A. L. Lombardi[51], M. Lorenzini[58], V. Loriette[108], M. Lormand[6], G. Losurdo[44], J. Lough[24], J. Luan[61], M. J. Lubinski[25], H. Lück[8,13], A. P. Lundgren[8], J. Macarthur[26], E. Macdonald[7], B. Machenschalk[8], M. MacInnis[10], D. M. Macleod[7], F. Magana-Sandoval[18], M. Mageswaran[1], K. Mailand[1], E. Majorana[19], I. Maksimovic[108], V. Malvezzi[58], N. Man[38], G. M. Manca[8], I. Mandel[20], V. Mandic[72], V. Mangano[19,67], M. Mantovani[14], F. Marchesoni[43,109], F. Marion[3], S. Márka[28], Z. Márka[28], A. Markosyan[29], E. Maros[1], J. Marque[23], F. Martelli[44,45], I. W. Martin[26], R. M. Martin[16], L. Martinelli[38], D. Martynov[1], J. N. Marx[1], K. Mason[10], A. Masserot[3], T. J. Massinger[24], F. Matichard[10], L. Matone[28], R. A. Matzner[110], N. Mavalvala[10], G. May[2], N. Mazumder[96], G. Mazzolo[8], R. McCarthy[25], D. E. McClelland[64], S. C. McGuire[111], G. McIntyre[1], J. McIver[51], D. Meacher[38], G. D. Meadors[56], M. Mehmet[8], J. Meidam[9], T. Meier[13], A. Melatos[105], G. Mendell[25], R. A. Mercer[12], S. Meshkov[1], C. Messenger[26], M. S. Meyer[6], H. Miao[61], C. Michel[41], E. E. Mikhailov[90], L. Milano[4,53], J. Miller[64], Y. Minenkov[58], C. M. F. Mingarelli[20], S. Mitra[75], V. P. Mitrofanov[34], G. Mitselmakher[16], R. Mittleman[10], B. Moe[12], M. Mohan[23], S. R. P. Mohapatra[24,57], F. Mokler[8], D. Moraru[25], G. Moreno[25], N. Morgado[41], T. Mori[83], S. R. Morriss[32], K. Mossavi[8], B. Mours[3], C. M. Mow-Lowry[8], C. L. Mueller[16], G. Mueller[16], S. Mukherjee[32], A. Mullavey[2], J. Munch[91], D. Murphy[28], P. G. Murray[26], A. Mytidis[16], M. F. Nagy[74], D. Nanda Kumar[16], I. Nardecchia[19,67], T. Nash[1], L. Naticchioni[19,67], R. Nayak[112], V. Necula[16], I. Neri[43,84], G. Newton[26], T. Nguyen[64], E. Nishida[83], A. Nishizawa[83], A. Nitz[24], F. Nocera[23], D. Nolting[6], M. E. Normandin[32], L. K. Nuttall[7], E. Ochsner[12], J. O'Dell[85], E. Oelker[10], G. H. Ogin[1], J. J. Oh[113], S. H. Oh[113], F. Ohme[7], P. Oppermann[8], B. O'Reilly[6], W. Ortega Larcher[32], R. O'Shaughnessy[12], C. Osthelder[1], D. J. Ottaway[91], R. S. Ottens[16], J. Ou[59], H. Overmier[6], B. J. Owen[81], C. Padilla[18], A. Pai[96], C. Palomba[19], Y. Pan[50], C. Pankow[12], F. Paoletti[14,23], R. Paoletti[14,15], M. A. Papa[12,21], H. Paris[25], A. Pasqualetti[23], R. Passaquieti[14,30], D. Passuello[14], M. Pedraza[1], P. Peiris[57], S. Penn[97], A. Perreca[24], M. Phelps[1], M. Pichot[38], M. Pickenpack[8], F. Piergiovanni[44,45], V. Pierro[68,69], L. Pinard[41], B. Pindor[105], I. M. Pinto[68,69], M. Pitkin[26], J. Poeld[8], R. Poggiani[14,30], V. Poole[42], C. Poux[1], V. Predoi[7], T. Prestegard[72], L. R. Price[1], M. Prijatelj[8], M. Principe[68,69], S. Privitera[1], R. Prix[8], G. A. Prodi[76,77], L. Prokhorov[34], O. Puncken[32], M. Punturo[43], P. Puppo[19], V. Quetschke[32], E. Quintero[1], R. Quitzow-James[46], F. J. Raab[25], D. S. Rabeling[9,49], I. Rácz[74], H. Radkins[25], P. Raffai[28,82], S. Raja[114], G. Rajalakshmi[115], M. Rakhmanov[32], C. Ramet[6], P. Rapagnani[19,67], V. Raymond[1], V. Re[58,66], C. M. Reed[25], T. Reed[116], T. Regimbau[38], S. Reid[117], D. H. Reitze[1,16], F. Ricci[19,67], R. Riesen[6], K. Riles[56], N. A. Robertson[1,26], F. Robinet[35], A. Rocchi[58], S. Roddy[6], C. Rodriguez[79], M. Rodruck[25], C. Roever[8], L. Rolland[3], J. G. Rollins[1], J. D. Romano[32], R. Romano[4,5], G. Romanov[90], J. H. Romie[6], D. Rosińska[31,118], S. Rowan[26], A. Rüdiger[8], P. Ruggi[23], K. Ryan[25], F. Salemi[8], L. Sammut[105], V. Sandberg[25], J. Sanders[56], V. Sannibale[1], I. Santiago-Prieto[26], E. Saracco[41], B. Sassolas[41], B. S. Sathyaprakash[7], P. R. Saulson[24], R. Savage[25], R. Schilling[8], R. Schnabel[8,13], R. M. S. Schofield[46], E. Schreiber[8], D. Schuette[8], B. Schulz[8], B. F. Schutz[7,21], P. Schwinberg[25], J. Scott[26], S. M. Scott[64], F. Seifert[1], D. Sellers[6], A. S. Sengupta[119], D. Sentenac[23], A. Sergeev[98], D. Shaddock[64], S. Shah[9,120], M. S. Shahriar[79], M. Shaltev[8], B. Shapiro[29], P. Shawhan[50], D. H. Shoemaker[10], T. L. Sidery[20], K. Siellez[38], X. Siemens[12], D. Sigg[25], D. Simakov[8], A. Singer[1], L. Singer[1], A. M. Sintes[52], G. R. Skelton[12], B. J. J. Slagmolen[64], J. Slutsky[8], J. R. Smith[18], M. R. Smith[1], R. J. E. Smith[20], N. D. Smith-Lefebvre[1], K. Soden[12], E. J. Son[113], B. Sorazu[26], T. Souradeep[75], L. Sperandio[58,66], A. Staley[28], E. Steinert[25], J. Steinlechner[8], S. Steinlechner[8], S. Steplewski[42], D. Stevens[79], A. Stochino[64], R. Stone[32], K. A. Strain[26], S. Strigin[34], A. S. Stroeer[32], R. Sturani[44,45], A. L. Stuver[6], T. Z. Summerscales[121], S. Susmithan[37], P. J. Sutton[7], B. Swinkels[23], G. Szeifert[82], M. Tacca[27], D. Talukder[46], L. Tang[32], D. B. Tanner[16], S. P. Tarabrin[8], R. Taylor[1], A. P. M. ter Braack[9], M. P. Thirugnanasambandam[1], M. Thomas[6], P. Thomas[25], K. A. Thorne[6], K. S. Thorne[61], E. Thrane[1], V. Tiwari[16], K. V. Tokmakov[107], C. Tomlinson[73], A. Toncelli[14,30], M. Tonelli[14,30], O. Torre[14,15], C. V. Torres[32], C. I. Torrie[1,26], F. Travasso[43,84], G. Traylor[6], M. Tse[28], D. Ugolini[122], C. S. Unnikrishnan[115], H. Vahlbruch[13], G. Vajente[14,30], M. Vallisneri[61], J. F. J. van den Brand[9,49], C. Van Den Broeck[9], S. van der Putten[9], M. V. van der Sluys[79], J. van Heijningen[9], A. A. van Veggel[26], S. Vass[1], M. Vasúth[74], R. Vaulin[10], A. Vecchio[20], G. Vedovato[123], J. Veitch[9], P. J. Veitch[91], K. Venkateswara[124], D. Verkindt[3], S. Verma[37], F. Vetrano[44,45], A. Viceré[44,45], R. Vincent-Finley[111], J.-Y. Vinet[38], S. Vitale[9,10], B. Vlcek[12], T. Vo[25], H. Vocca[43,84], C. Vorvick[25], W. D. Vousden[20], D. Vrinceanu[32], S. P. Vyachanin[34], A. Wade[64], L. Wade[12], M. Wade[12], S. J. Waldman[10], M. Walker[2], L. Wallace[1], Y. Wan[55], J. Wang[59], M. Wang[20], X. Wang[55], A. Wanner[8], R. L. Ward[64], M. Was[8], B. Weaver[25], L.-W. Wei[38], M. Weinert[8], A. J. Weinstein[1], R. Weiss[10], T. Welborn[6], L. Wen[37], P. Wessels[8], M. West[24], T. Westphal[8], K. Wette[8], J. T. Whelan[57], S. E. Whitcomb[1,37], D. J. White[73], B. F. Whiting[16], S. Wibowo[12], K. Wiesner[8], C. Wilkinson[25], L. Williams[16], R. Williams[1], T. Williams[125], J. L. Willis[126], B. Willke[8,13], M. Wimmer[8], L. Winkelmann[8], W. Winkler[8], C. C. Wipf[10], H. Wittel[8], G. Woan[26], J. Worden[25], J. Yablon[79], I. Yakushin[6], H. Yamamoto[1], C. C. Yancey[50], H. Yang[61], D. Yeaton-Massey[1], S. Yoshida[125], H. Yum[79], M. Yvert[3], A. Zadrożny[102], M. Zanolin[86], J.-P. Zendri[123], F. Zhang[10], L. Zhang[1], C. Zhao[37], H. Zhu[81], X. J. Zhu[37], N. Zotov[116,145], M. E. Zucker[10], and J. Zweizig[1]

(The LIGO Scientific Collaboration and the Virgo Collaboration)

and
C. Akerlof[56], C. Baltay[127], J. S. Bloom[128], Y. Cao[78], S. B. Cenko[36], A. Ćwiek[102], M. Ćwiok[129], V. Dhillon[73], D. B. Fox[81], A. Gal-Yam[130], M. M. Kasliwal[131,146], A. Klotz[132], M. Laas-Bourez[37,39], R. R. Laher[78], N. M. Law[133], A. Majcher[102], K. Małek[134,135], L. Mankiewicz[135], K. Nawrocki[102], S. Nissanke[78], P. E. Nugent[128,136], E. O. Ofek[130], R. Opiela[135], L. Piotrowski[129,137], D. Poznanski[138], D. Rabinowitz[127], S. Rapoport[64], J. W. Richards[128], B. Schmidt[139], M. Siudek[135], M. Sokołowski[102,140,141], I. A. Steele[142], M. Sullivan[143], A. F. Żarnecki[129], and W. Zheng[128]
[1] LIGO - California Institute of Technology, Pasadena, CA 91125, USA
[2] Louisiana State University, Baton Rouge, LA 70803, USA
[3] Laboratoire d'Annecy-le-Vieux de Physique des Particules (LAPP), Université de Savoie, CNRS/IN2P3, F-74941 Annecy-le-Vieux, France
[4] INFN, Sezione di Napoli, Complesso Universitario di Monte S. Angelo, I-80126 Napoli, Italy
[5] Università di Salerno, Fisciano, I-84084 Salerno, Italy
[6] LIGO - Livingston Observatory, Livingston, LA 70754, USA
[7] Cardiff University, Cardiff, CF24 3AA, UK
[8] Albert-Einstein-Institut, Max-Planck-Institut für Gravitationsphysik, D-30167 Hannover, Germany
[9] Nikhef, Science Park, 1098 XG Amsterdam, The Netherlands
[10] LIGO - Massachusetts Institute of Technology, Cambridge, MA 02139, USA
[11] Instituto Nacional de Pesquisas Espaciais, 12227-010 - São José dos Campos, SP, Brazil
[12] University of Wisconsin–Milwaukee, Milwaukee, WI 53201, USA
[13] Leibniz Universität Hannover, D-30167 Hannover, Germany
[14] INFN, Sezione di Pisa, I-56127 Pisa, Italy
[15] Università di Siena, I-53100 Siena, Italy
[16] University of Florida, Gainesville, FL 32611, USA
[17] The University of Mississippi, University, MS 38677, USA
[18] California State University Fullerton, Fullerton, CA 92831, USA
[19] INFN, Sezione di Roma, I-00185 Roma, Italy
[20] University of Birmingham, Birmingham, B15 2TT, UK
[21] Albert-Einstein-Institut, Max-Planck-Institut für Gravitationsphysik, D-14476 Golm, Germany
[22] Montana State University, Bozeman, MT 59717, USA
[23] European Gravitational Observatory (EGO), I-56021 Cascina, Pisa, Italy
[24] Syracuse University, Syracuse, NY 13244, USA
[25] LIGO - Hanford Observatory, Richland, WA 99352, USA
[26] SUPA, University of Glasgow, Glasgow, G12 8QQ, UK
[27] APC, AstroParticule et Cosmologie, Université Paris Diderot, CNRS/IN2P3, CEA/Irfu, Observatoire de Paris, Sorbonne Paris Cité, 10, rue Alice Domon et Léonie Duquet, F-75205 Paris Cedex 13, France
[28] Columbia University, New York, NY 10027, USA
[29] Stanford University, Stanford, CA 94305, USA
[30] Università di Pisa, I-56127 Pisa, Italy
[31] CAMK-PAN, 00-716 Warsaw, Poland
[32] The University of Texas at Brownsville, Brownsville, TX 78520, USA
[33] San Jose State University, San Jose, CA 95192, USA
[34] Moscow State University, Moscow 119992, Russia
[35] LAL, Université Paris-Sud, IN2P3/CNRS, F-91898 Orsay, France
[36] NASA/Goddard Space Flight Center, Greenbelt, MD 20771, USA
[37] University of Western Australia, Crawley, WA 6009, Australia
[38] ARTEMIS UMR 7250, Université Nice-Sophia-Antipolis, CNRS, Observatoire de la Côte d'Azur, F-06304 Nice, France
[39] Observatoire de Haute-Provence, CNRS, F-04870 Saint Michel l'Observatoire, France
[40] Institut de Physique de Rennes, CNRS, Université de Rennes 1, F-35042 Rennes, France
[41] Laboratoire des Matériaux Avancés (LMA), IN2P3/CNRS, Université de Lyon, F-69622 Villeurbanne, Lyon, France
[42] Washington State University, Pullman, WA 99164, USA
[43] INFN, Sezione di Perugia, I-06123 Perugia, Italy
[44] INFN, Sezione di Firenze, I-50019 Sesto Fiorentino, Firenze, Italy
[45] Università degli Studi di Urbino "Carlo Bo," I-61029 Urbino, Italy
[46] University of Oregon, Eugene, OR 97403, USA
[47] Laboratoire Kastler Brossel, ENS, CNRS, UPMC, Université Pierre et Marie Curie, F-75005 Paris, France
[48] Astronomical Observatory Warsaw University, 00-478 Warsaw, Poland
[49] VU University Amsterdam, 1081 HV Amsterdam, The Netherlands
[50] University of Maryland, College Park, MD 20742, USA
[51] University of Massachusetts–Amherst, Amherst, MA 01003, USA
[52] Universitat de les Illes Balears, E-07122 Palma de Mallorca, Spain
[53] Università di Napoli "Federico II," Complesso Universitario di Monte S. Angelo, I-80126 Napoli, Italy
[54] Canadian Institute for Theoretical Astrophysics, University of Toronto, Toronto, Ontario, M5S 3H8, Canada
[55] Tsinghua University, Beijing 100084, China
[56] University of Michigan, Ann Arbor, MI 48109, USA
[57] Rochester Institute of Technology, Rochester, NY 14623, USA
[58] INFN, Sezione di Roma Tor Vergata, I-00133 Roma, Italy
[59] National Tsing Hua University, Hsinchu 300, Taiwan
[60] Charles Sturt University, Wagga Wagga, NSW 2678, Australia
[61] Caltech-CaRT, Pasadena, CA 91125, USA
[62] INFN, Sezione di Genova, I-16146 Genova, Italy
[63] Pusan National University, Busan 609-735, Korea
[64] Australian National University, Canberra, ACT 0200, Australia
[65] Carleton College, Northfield, MN 55057, USA
[66] Università di Roma Tor Vergata, I-00133 Roma, Italy
[67] Università di Roma "La Sapienza," I-00185 Roma, Italy

[68] University of Sannio at Benevento, I-82100 Benevento, Italy
[69] INFN (Sezione di Napoli), Italy
[70] The George Washington University, Washington, DC 20052, USA
[71] University of Cambridge, Cambridge, CB2 1TN, UK
[72] University of Minnesota, Minneapolis, MN 55455, USA
[73] The University of Sheffield, Sheffield S10 2TN, UK
[74] Wigner RCP, RMKI, H-1121 Budapest, Konkoly Thege Miklós út 29-33, Hungary
[75] Inter-University Centre for Astronomy and Astrophysics, Pune-411007, India
[76] INFN, Gruppo Collegato di Trento, I-38050 Povo, Trento, Italy
[77] Università di Trento, I-38050 Povo, Trento, Italy
[78] California Institute of Technology, Pasadena, CA 91125, USA
[79] Northwestern University, Evanston, IL 60208, USA
[80] Montclair State University, Montclair, NJ 07043, USA
[81] The Pennsylvania State University, University Park, PA 16802, USA
[82] MTA-Eotvos University, "Lendulet" A. R. G., Budapest 1117, Hungary
[83] National Astronomical Observatory of Japan, Tokyo 181-8588, Japan
[84] Università di Perugia, I-06123 Perugia, Italy
[85] Rutherford Appleton Laboratory, HSIC, Chilton, Didcot, Oxon, OX11 0QX, UK
[86] Embry-Riddle Aeronautical University, Prescott, AZ 86301, USA
[87] Perimeter Institute for Theoretical Physics, Ontario, N2L 2Y5, Canada
[88] American University, Washington, DC 20016, USA
[89] University of New Hampshire, Durham, NH 03824, USA
[90] College of William and Mary, Williamsburg, VA 23187, USA
[91] University of Adelaide, Adelaide, SA 5005, Australia
[92] Raman Research Institute, Bangalore, Karnataka 560080, India
[93] Korea Institute of Science and Technology Information, Daejeon 305-806, Korea
[94] Białystok University, 15-424 Białystok, Poland
[95] University of Southampton, Southampton, SO17 1BJ, UK
[96] IISER-TVM, CET Campus, Trivandrum Kerala 695016, India
[97] Hobart and William Smith Colleges, Geneva, NY 14456, USA
[98] Institute of Applied Physics, Nizhny Novgorod 603950, Russia
[99] Seoul National University, Seoul 151-742, Korea
[100] Hanyang University, Seoul 133-791, Korea
[101] IM-PAN, 00-956 Warsaw, Poland
[102] NCBJ, 05-400 Świerk-Otwock, Poland
[103] Institute for Plasma Research, Bhat, Gandhinagar 382428, India
[104] Utah State University, Logan, UT 84322, USA
[105] The University of Melbourne, Parkville, VIC 3010, Australia
[106] University of Brussels, Brussels 1050, Belgium
[107] SUPA, University of Strathclyde, Glasgow, G1 1XQ, UK
[108] ESPCI, CNRS, F-75005 Paris, France
[109] Dipartimento di Fisica, Università di Camerino, I-62032 Camerino, Italy
[110] The University of Texas at Austin, Austin, TX 78712, USA
[111] Southern University and A&M College, Baton Rouge, LA 70813, USA
[112] IISER-Kolkata, Mohanpur, West Bengal 741252, India
[113] National Institute for Mathematical Sciences, Daejeon 305-390, Korea
[114] RRCAT, Indore, MP 452013, India
[115] Tata Institute for Fundamental Research, Mumbai 400005, India
[116] Louisiana Tech University, Ruston, LA 71272, USA
[117] SUPA, University of the West of Scotland, Paisley, PA1 2BE, UK
[118] Institute of Astronomy, 65-265 Zielona Góra, Poland
[119] Indian Institute of Technology, Gandhinagar, Ahmedabad, Gujarat 382424, India
[120] Department of Astrophysics/IMAPP, Radboud University Nijmegen, P.O. Box 9010, 6500 GL Nijmegen, The Netherlands
[121] Andrews University, Berrien Springs, MI 49104, USA
[122] Trinity University, San Antonio, TX 78212, USA
[123] INFN, Sezione di Padova, I-35131 Padova, Italy
[124] University of Washington, Seattle, WA 98195, USA
[125] Southeastern Louisiana University, Hammond, LA 70402, USA
[126] Abilene Christian University, Abilene, TX 79699, USA
[127] Yale University, New Haven, CT 06520, USA
[128] University of California Berkeley, Berkeley, CA 94720, USA
[129] Faculty of Physics, University of Warsaw, Hoza 69, 00-681 Warsaw, Poland
[130] Weizmann Institute of Science, 76100 Rehovot, Israel
[131] Observatories of the Carnegie Institution for Science, Pasadena, CA 91101, USA
[132] Institut de Recherche en Astrophysique et Planetologie (IRAP), F-31400 Toulouse, France
[133] Department of Physics and Astronomy, University of North Carolina at Chapel Hill, Chapel Hill, NC 27599-3255, USA
[134] Division of Particles and Astrophysical Science, Nagoya University, Furo-cho, Chikusa-ku, 464-8601 Nagoya, Japan
[135] Centre for Theoretical Physics of Polish Academy of Sciences, Al. Lotnikow 32/46, 02-668 Warsaw, Poland
[136] Lawrence Berkeley National Laboratory, Berkeley, CA 94720, USA
[137] RIKEN, 2-1 Hirosawa, Wako, 351-0198, Saitama, Japan
[138] School of Physics and Astronomy, Tel Aviv University, Tel Aviv 69978, Israel
[139] The Research School of Astronomy and Astrophysics, The Australian National University, via Cotter Rd, Weston Creek, ACT 2611, Australia
[140] International Centre for Radio Astronomy Research-Curtin University, GPO Box U1987, Perth, WA 6845, Australia
[141] ARC Centre of Excellence for All-sky Astrophysics (CAASTRO)
[142] Astrophysics Research Institute, Liverpool John Moores University, L3 5RF, UK
[143] School of Physics and Astronomy, University of Southampton, Highfield, Southampton, SO17 1BJ, UK
Received 2013 October 30; accepted 2014 January 18; published 2014 February 11

ABSTRACT

During the Laser Interferometer Gravitational-wave Observatory and Virgo joint science runs in 2009–2010, gravitational wave (GW) data from three interferometer detectors were analyzed within minutes to select GW candidate events and infer their apparent sky positions. Target coordinates were transmitted to several telescopes for follow-up observations aimed at the detection of an associated optical transient. Images were obtained for eight such GW candidates. We present the methods used to analyze the image data as well as the transient search results. No optical transient was identified with a convincing association with any of these candidates, and none of the GW triggers showed strong evidence for being astrophysical in nature. We compare the sensitivities of these observations to several model light curves from possible sources of interest, and discuss prospects for future joint GW-optical observations of this type.

Key words: binaries: close – catalogs – gravitational waves – stars: neutron – surveys

Online-only material: color figures

1. INTRODUCTION

Transient gravitational-wave (GW) emission is expected from highly energetic astrophysical events such as stellar-core collapses and mergers of binary neutron stars (NSs). The Laser Interferometer Gravitational-wave Observatory (LIGO; Abbott et al. 2009; Harry et al. 2010) includes detectors located in the United States near Hanford, Washington (H1) and Livingston, LA (L1). A similarly designed Virgo (V1; Accadia et al. 2012; Virgo Collaboration 2009) detector is located in Italy near the city of Cascina. Each interferometer contains a pair of perpendicular arms, 4 km long in the LIGO detectors and 3 km in Virgo, whose effective optical path length is slightly altered by passing GW signals. Since 2007, LIGO and Virgo have coordinated operations and shared data, so the three sites operate as a single network of detectors seeking direct measurements of GW signals. A fourth site, GEO600 in Hannover, Germany (Grote et al. 2008), also shares data with LIGO and Virgo.

During the 2009–2010 science run of the LIGO/Virgo network (Abadie et al. 2012e) we implemented low-latency searches for GW transients. The analysis software identified GW event candidates ("triggers"), estimated their statistical significance, and reconstructed likely source positions in approximately 10 minutes. Alert messages were transmitted to a network of electromagnetic observatories after the manual validation of the GW triggers with a total latency of ∼30 minutes. The collection of optical telescopes, as well as the *Swift* satellite, LOFAR, and the Expanded Very Large Array (Lazio et al. 2012), provided target of opportunity follow-up observations to the GW triggers. In earlier publications, we described the search method and likely sources of both GW and emission measure (EM) transients (Abadie et al. 2012c, 2012d), as well as the results of the follow-up observations performed with the *Swift* satellite (Evans et al. 2012).

In this paper, we describe the data set collected with optical telescopes, detail the methods used to search the data for transients consistent with expected optical counterparts to GWs, and report the results of this analysis. In this first effort to use optical instruments to search for transients based on data from GW detectors, none of the GW triggers showed strong evidence for being astrophysical in nature. However, searching for transients in a large sky area is a challenging problem, and uncertainty in the expected light curve and spectrum of the sought optical counterpart makes the problem harder still. For this reason, we emphasize the methodologies used to identify transient phenomena in our data set and to separate objects consistent with our target models from those that are not. In addition, we discuss the results of Monte Carlo simulations used to test the efficiency of our pipelines in recovering various types of transients, and the implications for future searches of optical counterparts of GW events discovered with next generation observatories.

A variety of astrophysical processes are likely to be associated with both GW and EM emission. Among these, gamma-ray bursts (GRBs) are promising sources for joint GW and EM studies (e.g., Kochanek & Piran 1993; Kobayashi & Mészáros 2003; Abadie et al. 2012b). GRBs are traditionally divided in two main classes, long and short bursts (Kouveliotou et al. 1993), which are thought to be associated with different progenitors (e.g., Gehrels et al. 2007; Mészáros 2006, and references therein). Long GRBs are associated with "collapsars," the gravitational collapse of cores of massive stars (Woosley 1993; MacFadyen & Woosley 1999), while short GRBs may be produced by mergers of binary systems of compact objects (NS/NS or black-hole/NS; e.g., Eichler et al. 1989; Paczynski 1991; Narayan et al. 1992). A compact binary merger results from gravitational radiation, producing a characteristic "inspiral" of the binary orbit and a corresponding strong GW signal (e.g., Thorne 1987; Shibata & Taniguchi 2011). GW emission from a collapsar depends on non-spherically-symmetric flow of material during the collapse, which may be enhanced by centrifugal effects if the progenitor is rotating rapidly (Davies et al. 2002; Fryer et al. 2002; Shibata et al. 2003; Piro & Pfahl 2007; Corsi & Mészáros 2009; Ott 2009; Romero et al. 2010).

High-energy emission from GRBs is thought to escape as narrow relativistic jets (e.g., Sari et al. 1999; Harrison et al. 1999; Frail et al. 2001; Racusin et al. 2009), though at least in the case of the short GRBs, there is uncertainty regarding the angular extent of typical beams (Fong et al. 2012), as well as how the beaming angle depends on wavelength (van Eerten & MacFadyen 2011). Afterglows of both classes of GRBs have been observed over a wide range of wavelengths (Costa et al. 1997; Frail et al. 1997; van Paradijs et al. 1997; Gehrels et al. 2005; Hjorth et al. 2005; Abdo et al. 2009), from times nearly concurrent with the prompt emission to days later (e.g., Nousek et al. 2006; Molinari et al. 2007; Racusin et al. 2011, and references therein). Generally, the observed optical afterglows fade with a temporal power-law decay, with typical indices between 1 and 1.5 (e.g., Sari et al. 1998; Nakar 2007). A wide range of luminosities have been observed, with the afterglows of short bursts tending to be less energetic than the afterglows of long bursts (Kann et al. 2011).

[144] Deceased, 2012 April.
[145] Deceased, 2012 May.
[146] Hubble Fellow and Carnegie-Princeton Fellow.

Table 1
R-band Light Curve Models Used for Simulated Injections

Source	Light Curve Model		Normalization Condition
Short GRB	$L \propto t^{-1.1}$		23–31 mag at 1 day from $z = 1$
Long GRB	$L \propto t^{-1.1}$		16–24 mag at 1 day from $z = 1$
Kilonova	$L = (1.2 \times 10^{42}) t^{0.43}$ erg s^{-1}	$t < 0.7$ days	
	$L = (6.7 \times 10^{41}) t^{-1.29}$ erg s^{-1}	$t > 0.7$ days	

Notes. Normalizations used for the on-axis short GRB and long GRB models correspond to the full range of observed on-axis GRB afterglows in each class in the observer frame, assuming $z = 1$, from Kann et al. (2010, 2011). The kilonova model is intended to mimic the light curves shown in Metzger et al. (2010) and Piran et al. (2013).

The merger of two NSs or a NS with a black hole may lead to a supernova-like transient, as described by Li & Paczyński (1998). In their model, heavy radioactive elements are formed in the merger ejecta through rapid neutron capture nucleosynthesis. As the newly formed isotopes decay toward stability, they release energy and heat the ejecta. Thermal emission becomes visible after the ejecta has expanded enough to allow photons to escape. The expected transient, referred to as a kilonova throughout this paper, is roughly isotropic, and the associated light curve is expected to peak about a day after the merger time (Metzger et al. 2010; Piran et al. 2013). The model has been supported by a variety of computational work (Faber & Rasio 2012; Roberts et al. 2011), though some details of the model are still uncertain, including the amount of mass ejected from the merger and the physics of the radiative transport. These unknowns lead to uncertainties in the peak luminosity, time-scale, and color evolution of the model. For example, Barnes & Kasen (2013) found that the ejected NS material may have a high opacity, leading to light curves that peak in infrared rather than optical wavelengths; this prediction seems consistent with one recent observation (Tanvir et al. 2013; Berger et al. 2013). For testing purposes, we adopted a simple model which was intended to mimic the main features of the light curves in Metzger et al. (2010) and Piran et al. (2013) (see Table 1).

Core-collapse supernovae are expected to emit enough GW energy to be observable with current detectors within some fraction of the Milky Way, to distances of perhaps a few kpc (Ott 2009). A rare class of core-collapse supernovae is also known to be linked to long GRBs (Galama et al. 1998; Woosley & Bloom 2006; Soderberg et al. 2006). Indeed, optical follow-ups of GW triggers could catch optical supernovae harboring off-axis GRBs, whose gamma-ray emission would be missed because the relativistic GRB jet is not pointed toward earth (Granot et al. 2002; Rhoads 2003; van Eerten et al. 2010). However, unlike the models discussed above, tracking a supernova light curve requires several days or weeks of observations after the GW trigger (Doggett & Branch 1985). Slow light curves are also expected from off-axis GRBs, whose emission is expected to peak on timescales of weeks to months (e.g., van Eerten & MacFadyen 2011). Taking into account that the LIGO and Virgo detectors are expected to detect more merger events than core-collapse events, the cadence of our optical follow-up observations was chosen mainly for shorter optical transients, but with some observations extending to later times to possibly catch a slower transient.

The paper is organized as follows: Section 2 first gives a description of the ground-based telescopes involved in the follow-up program. In Section 3, we present the set of GW triggers that were selected and sent as alerts to the telescopes and we describe their associated follow-up observations. Section 4 details the methods employed to search for optical transients in the collected series of images and Section 5 reports the results of the searches. Finally, estimates of the search sensitivity are presented in Section 6.

2. TELESCOPES INVOLVED IN THE FOLLOW-UP PROGRAM

The optical follow-up program took place during times when the LIGO and Virgo observatories were operating in coincidence during 2009 and 2010. This time was divided into two segments: the "winter" run, between 2009 December and 2010 January, and the "autumn" run spanning most of 2010 September and October. The program was executed as a joint study between the LIGO and Virgo collaborations, and about 10 teams which operated automated and remotely controlled telescopes.

During the winter run, triggers from the LIGO/Virgo network were passed to the TAROT (Klotz et al. 2009) and QUEST (Baltay et al. 2007) telescopes. For the autumn run, the optical network was expanded to include Palomar Transient Factory (PTF; Rahmer et al. 2008; Law et al. 2009; Rau et al. 2009), Pi of the Sky (POTS; Malek et al. 2009), ROTSE III (Akerlof et al. 2003), SkyMapper (Keller et al. 2007), the Zadko Telescope (Coward et al. 2010), and the Liverpool Telescope (Steele et al. 2004). The large number (12) of telescopes participating in the autumn run allowed for better sky coverage. The main characteristics of these observatories are listed in Table 2. With the exception of the Liverpool RATCam and Zadko, they are all equipped with wide field cameras. A wide field of view (FOV) was considered an important feature for this study, due to the imprecise source localization of the GW instruments. We expected localizations of a few tens of square degrees up to 200 deg^2, and so instruments without a wide FOV would be unable to image a significant fraction of the uncertainty region (Cavalier et al. 2004; Nissanke et al. 2011; Fairhurst 2011; Klimenko et al. 2011). However, with the limited sensitive range to an optimally aligned source (horizon distance) of initial LIGO and Virgo, it was also possible for an instrument to observe only the most likely host galaxies for a compact object merger (Abadie et al. 2012d; Kanner et al. 2008; Nuttall & Sutton 2010).

Separate observing plans were constructed for each observatory. Some of the instruments targeted only the single most likely field for a given GW trigger, while others observed multiple fields in an effort to cover an area comparable to the GW position uncertainty (see Table 2). Planned cadences were also different for each observatory. Generally, the goal was to observe at least once as quickly as possible to image a potential rapidly fading counterpart. Where possible, attempts were made to image each field over several nights following the GW trigger, in order to trace the light curves of potential transients. The details of the observations are described in Section 5.

Table 2
Characteristics of Instruments Involved in the Search

Name	Locations	FOV (deg^2)	Aperture (m)	Exposure Time (s)	Limiting Magnitude	Tiles
Palomar Transient Factory	1	7.3	1.2	60	20.5	10
Pi of the Sky	1	400	0.072	10	11.5	1
QUEST	1	9.4	1	60	20.5	3
ROTSE III	4	3.4	0.45	20	17.5	1
SkyMapper	1	5.7	1.35	110	21.5	8
TAROT	2	3.4	0.25	180	17.5	1
Zadko Telescope	1	0.15	1	120	20.5	5
Liverpool Telescope - RATCam	1	0.0058	2	300	21	1
Liverpool Telescope - SkyCamZ	1	1	0.2	10	18	1

Notes. The column labeled "Tiles" indicates the maximum number of different field positions that the telescope searched in response to a trigger. The shown limiting magnitudes are estimates, under ideal observing conditions. They are listed in r' band for RATCam, r band for SkyMapper, and R band for all other instruments. Palomar Transient Factory, SkyMapper and RATCam are calibrated to the SDSS/AB photometric system; the others are expressed in the Vega photometric system.

3. GRAVITATIONAL-WAVE TRIGGERS SELECTED FOR FOLLOW-UP OBSERVATIONS

3.1. Trigger Selection

Triggers for this search were identified with a collection of low-latency pipelines designed to find transient GW events in data from the three site LIGO/Virgo network. Here, we provide a brief summary of the trigger production and selection, while a more detailed description is described in Abadie et al. (2012c, 2012d). During the winter run, two pipelines were used to identify generic short-duration transients of significant signal power, or "bursts," and estimate their source positions: the Omega (Ω) Pipeline (Searle et al. 2008; Abadie et al. 2010a) and the coherent WaveBurst (cWB) pipeline (Klimenko et al. 2011). For the autumn run, a third trigger pipeline was added: the Multi-Band Template Analysis (MBTA; Beauville et al. 2008; Abadie et al. 2012c), which sought inspiral waveforms from coalescing compact objects. The autumn run also added a second instance of cWB, configured to target linearly polarized GW signals, as might be expected from supernovae.

To compare triggers from different pipelines and identify the ones suitable for observation, follow-up software made event candidate selections based on the estimated false alarm rate (FAR) of each trigger. The rate of background false alarms was estimated by forming a distribution of artificial triggers from data with one or more data streams shifted by at least several seconds. Time-shifting data removes correlations of possible GW signals between detectors, so this distribution was considered to be free from any putative signals and represented the rate of triggers not due to transient GWs (Abadie et al. 2012a, 2012e). During the winter run, a FAR threshold of 1 trigger day^{-1} was applied to triggers, and a less significant FAR was accepted in the last week to exercise the system. For the autumn run, the FAR threshold was set to 0.25 day^{-1}. Triggers which passed the automated threshold received attention from an on-call follow-up team. The on-call team checked that the trigger occurred in high quality data in each interferometer. In addition, the criteria for manual validation in the winter run included demands that the three suggested (see below) QUEST fields covered a sky area corresponding to a greater than 50% probability of containing the GW source and that follow-up requests were sent at a rate of less than one per 24 hr.

The trigger pipelines reported the estimated position of each candidate GW event as a *skymap*, a list of probability densities assigned to pixels in a grid covering the sky. The grid used pixels approximately $0.^{\circ}4$ on a side, selected to be similar to the degree-scale resolving power of the GW network (for example, Fairhurst 2011; Klimenko et al. 2011; Vitale et al. 2012; Nissanke et al. 2011). The large angular size of the skymaps required a choice of where within the uncertainty region to observe. To observe the regions most likely to contain an observable GW source, we used a catalog of galaxies within 50 Mpc and Milky Way globular clusters (GWGC; White et al. 2011), thought to be around 70% complete to 50 Mpc by B-band luminosity. Each pixel in the skymap was given a weight P according to the formula

$$P \propto L\left(\frac{M}{D}\right), \quad (1)$$

where L is the probability of the pixel derived from the GW data alone; M is the blue light luminosity of the galaxy or galaxies contained in the pixel, which is used as a proxy for the star formation rate; and D is the distance to the galaxy (Nuttall & Sutton 2010). For MBTA triggers, a slightly modified version of this approach was applied, using the maximum distance consistent with the apparent inspiral signal (Abadie et al. 2012c). The suggested fields for each telescope were those that maximized the sum of P within the respective FOV. Unless unobservable due to daylight or geometrical constraints, the suggested fields were passed to each optical telescope for every GW event candidate that passed manual validation. However, a more stringent selection was applied for PTF, and only one GW trigger was sent to PTF.

3.2. Data Set

In the winter run, the on-call team was alerted a total of nine times. Three of these triggers were vetoed by the on-call team. Six triggers were approved by the on-call team and sent to the QUEST and TAROT telescopes with roughly 30 minutes of latency. Of the six requests, four were rejected as unobservable by the scheduling software of both telescopes and two triggers were followed-up with the QUEST telescope. In addition, two triggers that did not pass the automated FAR threshold were selected by the on-call team and passed to the partner observatories in an effort to expand the winter run data set (see Table 3).

In the autumn run, only one trigger was manually rejected due to data quality concerns. Six triggers resulted in alerts

Table 3
Gravitational Wave Triggers in the Winter Run

ID	Date	UTC	Pipeline	FAR (day^{-1})	Follow-up
G3821	2009 Dec 29	15:16:33	Ω	0.66	QUEST collected 12 images
CWB1	2010 Jan 3	20:37:22	cWB	1.3	Alert sent Jan 7; TAROT collected 6 images
G4202	2010 Jan 6	06:49:45	Ω	4.5	QUEST collected 9 images
CWB2	2010 Jan 7	08:46:37	cWB	1.6	QUEST collected 12 images

Table 4
Gravitational Wave Triggers in the Autumn Run

ID	Date	UTC	Pipeline	FAR (day^{-1})	Follow-up
G19377	2010 Sep 16	06:42:23	cWB (unmodeled)	<0.01	ROTSE collected 117 images, TAROT collected 20, Zadko 129, and SkyMapper 21. Blind injection
G20190	2010 Sep 19	12:02:25	MBTA	0.16	ROTSE collected 257 images, QUEST 23, Zadko 159, and TAROT 3
G21852	2010 Sep 26	20:24:32	cWB (linear)	0.02	ROTSE collected 130 images, PTF 149, CAT 3 DQ
G23004	2010 Oct 3	16:48:23	Ω	0.21	ROTSE collected 153 images, QUEST 40, Liverpool - RATCam 22, Liverpool - SkyCamZ 121, and POTS 444

to the observing partners, four of which resulted in follow-up observations[147] (see Table 4). Two of the triggers are worth special note. The September 16 trigger was recognized by the on-call team as having a special significance: in addition to a small estimated FAR, spectrograms of the GW data revealed frequency evolution characteristic of the late inspiral and merger of two compact objects. This event was later revealed to be a blind hardware injection, a simulated signal secretly added to the data to test the end-to-end system. The September 26 event candidate was also discovered with a low FAR estimate. In subsequent GW data analysis, this trigger was found to be the most significant cWB trigger above 200 Hz in the time period where H1, L1, and V1 were running in coincidence in this science run, though was removed from the analysis based on data quality concerns. The FAR was measured to be 0.023 events per day, or one such trigger expected for every 44 days of network livetime. Since these detectors ran in coincidence for a total of 52.2 days throughout the Virgo science run, this trigger was consistent with expectations for detector noise.

4. SEARCHES FOR OPTICAL TRANSIENTS

A search for optical transients essentially consists of searching for fading optical point sources in a sequence of astronomical images. A few characteristics make the search for GW counterparts unique. First, there is a significant uncertainty regarding the expected light curve from a GW source; we targeted short duration (hours to days) transients consistent with GRB afterglows and kilonovae light curves. Second, the poor localization of the GW error box required searching through a large portion of the sky. This significantly differed from the arcminute-scale error box used to find optical afterglows of GRBs discovered by *Swift*. Finally, we designed automated pipelines with Monte-Carlo simulations to evaluate the statistical significance of any apparent counterpart.

The telescopes involved in the program included very different instruments ranging from shallow, very wide-field cameras to meter-class telescopes (Table 2). They collected images with different cadences and follow-up strategies, leading to a heterogeneous data set. This has led us to develop a similarly heterogeneous analysis approach, with techniques tailored to match the requirements of each observational data set. Where possible, we leveraged existing software already in use by the various astronomical teams. The list of techniques which were applied in some, but not all, of the developed searches included image subtraction, identification of host galaxies, cuts on shape parameters, automated transient classifiers, volunteer work by citizen scientists, and consistency checks on light curve properties.

In future searches for optical counterparts to GW sources, a critical component will be rapidly down-selecting candidate lists to allocate follow-up resources such as large aperture photometry and spectroscopy. In this work, we attempted to unify results from disparate analyses by developing two common search statistics, which were applied in multiple analyses. The first statistic was used to quantify the ability to reject false positives, and labeled the "false-alarm probability" (FAP). The FAP was defined as the probability that a set of optical images taken with a given telescope in response to a single GW trigger, and analyzed with a given pipeline, would lead to a false positive. The FAP could encompass both false positives arising from technical noise, such as procedure artifacts, and astrophysical transients not related to the GW sources, such as M dwarf flares, Galactic variable stars, and extragalactic active galactic nuclei (AGNs) and supernovae. For most data sets, we set a FAP target of 10%. This FAP level was chosen to reduce the number of false positives to a manageable level, so that each object passing the selection criteria could, in principle, be further studied with sensitive photometric and/or spectroscopic observations. The second statistic used to characterize an analysis was the detection efficiency, defined as the recovery rate for simulated optical transients added to representative images. We measured detection efficiencies for a few different model light curves, using data and analysis procedures from several different telescopes. The FAP measurements and the Monte Carlo simulations allowed us to find a good compromise between rejection of false positives and reduction of interesting EM candidates. For example, in a study with the QUEST and TAROT data, we found that increasing the FAP to 0.20 would produce less than a 30% improvement in the sensitive distance range of the search, and so would increase the sensitive search volume by roughly a factor

[147] Of the two triggers not observed, one was the first alert generated during the autumn run and ROTSE imaged the wrong location due to a software bug, while the other was too close to the Sun to be observable by any of the telescopes.

of two, while also doubling the number of false positives. This section describes the different methods that were used to identify potential transients consistent with our models, and reduce false positives.

4.1. Catalog-based Search for TAROT, Zadko, and QUEST Observations

This section describes the image analysis pipeline developed specifically for the TAROT, Zadko Telescope, and QUEST observations. Unlike other approaches presented in this work, the pipeline did not use image subtraction but it extracted a source catalog from each image, and sought transients by comparing the set of catalogs to a reference. For this reason, we refer to this pipeline as the "catalog-based search."

4.1.1. Analysis Pipeline

The search consisted of three main steps applied to the image set (after dark, flat and sky background level corrections): data photometric calibration, reconstruction of object light curves, and transient selection to identify possible electromagnetic counterparts.

TAROT, the Zadko Telescope, and QUEST observed with a clear filter. The magnitude zero-point calibration was performed using the USNO-A2.0 catalog (Monet et al. 1998) as reference and resulted in red equivalent magnitudes. For the QUEST camera, which is composed of 112 individual CCDs, calibration was performed separately on each CCD. The different response, data quality, and sensitivity of each CCD prevented managing them as a single mosaic, and the data analysis was performed CCD by CCD.

The source catalog of each image was extracted using `SExtractor` (Bertin & Arnouts 1996). Each list of sources was spatially cross-correlated with the star catalog USNO-A2.0 using the tool `match` (Droege et al. 2006). The radius used to search for common sources was set to 10″ for TAROT, 2″ for Zadko, and 3″ for QUEST. These values took into account the positional uncertainties in the images and in the USNO-A2.0 catalog. Sources found to coincide in position and luminosity with objects listed in the reference catalog were excluded from the search. The lists of remaining sources were then mutually cross-correlated in position to link sources observed at different times to common astrophysical objects. This resulted in a light curve for each identified object.

At this point, two types of analyses were conducted to select GW associated transients and reject background objects. The *on-source analysis* was restricted to objects lying in the image regions associated with galaxies within 50 Mpc[148] and Galactic globular clusters. For each galaxy a circular region with a radius five times the galaxy's semi-major axis (as provided by the GWGC; White et al. 2011) was analyzed. This region (which corresponds to an average radius of about 20 kpc) accounted for the typical projected physical offsets observed between GRB afterglows and their host galaxy centers (e.g., Berger 2010). The *whole-field analysis* covered the entire FOV but was limited to bright objects. For the QUEST telescope, large variations in the sensitivity and image quality between different CCDs made setting a whole-field magnitude threshold unfeasible to search the expected counterparts. For this reason, we performed only the on-source analysis on the QUEST data, which allowed us to search for faint transients while limiting the number of false positives (see Section 4.1.2).

For both types of analysis, rapid contaminating transients, including cosmic rays, asteroids, and CCD noise, were rejected by requiring the presence of the object in a minimum number of consecutive images. Further selection of transient objects (and hence rejection of background) was performed by applying thresholds to the initial (first observation) magnitude and light curve variability of each source. Variability was characterized by assuming power-law luminosity dimming with time, $\mathcal{L} \propto t^{-\beta}$, corresponding to a linear magnitude variation $m = 2.5\beta \log_{10}(t) + C$. The slope index 2.5β was evaluated for each object. The expected slope indices for GRB afterglows and kilonova light curves are around 2.5–4 (see Table 1). To seek these transients, we applied a cut which selected slope indices greater than 0.5. Because of the small number of repeated observations with QUEST (maximum of eight for each galaxy), a different variability measurement was used for this instrument's analysis. A threshold on the flux variation between the first and the following nights of observation was set by requiring a dimming larger than +0.5 mag (while we expected >+1 based on the light curve models and the QUEST observational cadence).

Studies of the background events (Section 4.1.2) and the ability to detect simulated on-axis GRBs and kilonovae (Section 6) were used to design selection criteria yielding a FAP of under 10% (prior probability that a background event passes all the selection criteria), while also accepting a wide range of astrophysical models. The thresholds applied to the variability measure (slope index or flux variation) were designed to detect fading transients while leaving the possibility of detecting light curves showing flaring within short time-scales (hours). However, recent re-evaluations of kilonova emission by Barnes & Kasen (2013) and others have indicated that more realistic values for the opacities of the heavy radioactive elements lead to dimmer and broader light curves. These would be difficult to detect with the depth and cadence of our data set.

4.1.2. Background Estimation

The background was estimated by running the analysis over a series of images obtained from random time permutations of the real observation images. The first night observations were excluded from being selected as the first image in each permuted sequence to remove any astrophysical electromagnetic counterparts from the data set. The background simulation was repeated 100 times for TAROT and the Zadko Telescope and for all the permutations allowed by the observations for QUEST.

Genuine optical transients would have lost their regularly fading light curve in the scrambled image set. Random sequencing thus erased them while artifacts such as CCD noise, pixel saturation, bad pixels, errors in the de-blending and source association, etc., were just as likely to pass the pipeline's selection cuts as with the true sequencing. This procedure allowed a measurement of the rate of false positives due to "technical" noise. However, this procedure did not permit a valuable estimate of the "astrophysical" background since the randomization reduced the number of identified astrophysical transients that actually dimmed over time. A statistically significant estimate of the astrophysical background would require the study of survey data not associated with GW triggers, which was not available at this time.

An example of the distribution of technical background events (after the removal of rapid transients) detected in the FOV of TAROT for trigger G19377 is shown in Figure 1. The cumulative

[148] Except for trigger G20190, for which we selected galaxies within 30 Mpc in accordance with the gravitational wave horizon estimated for this event candidate.

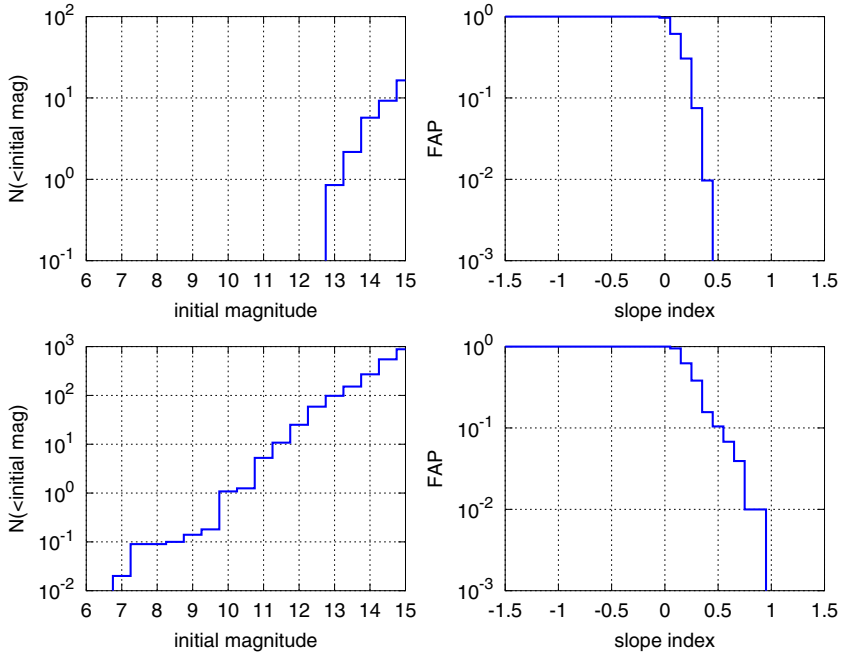

Figure 1. Background plots for TAROT data associated with trigger G19377 obtained by performing the *on-source analysis* (top plots) and *whole-field analysis* (bottom plots). In the left plots, *N* gives the cumulative number of technical background events found in a permuted set of images above the magnitude threshold shown on the *X*-axis, averaged over 100 permutations. The right plots show the FAP as a function of the slope index (in the case of *whole-field analysis* the requirement of an initial magnitude brighter than 14 was applied).

(A color version of this figure is available in the online journal.)

distribution of their initial magnitude is shown in the left plot, and the FAP as a function of the slope index is in the central plot. The on-source analysis showed a greatly reduced background level compared to the whole-field analysis, since only objects near a local galaxy were included. In this example, the nominal slope index threshold of 0.5 reduced the FAP to less than 1% in the on-source analysis. For the whole-field analysis, in addition to the same cut on slope index, a requirement that objects showed an initial flux brighter than magnitude 14 was needed to reduce the FAP below the 10% objective.

The "technical background" rate varied significantly between different instruments due to different fields of view, limiting magnitudes, image quality, and star crowding. For TAROT and Zadko, the number per square degree of "technical false positives" brighter than a reference magnitude of 14.5 mag for TAROT and 15.5 mag for Zadko was evaluated to be less than 1 deg^{-2} using a slope index threshold of 0.5. For QUEST, the background study was performed CCD by CCD to account for the different density of false positives on each CCD. Compared to TAROT and Zadko, the deeper sensitivity observations of QUEST led to a higher number of false positives: an average value of 6 deg^{-2} brighter than 18 mag and with magnitude variation larger than 0.5. Reducing the analysis to the on-source regions allowed us to lower the density of background transients to less than 1 deg^{-2}.

4.1.3. Analysis Tuning

For TAROT and Zadko the two types of analysis were tuned to achieve 10% FAP using the on-source and whole-field backgrounds, respectively. The nominal slope index threshold (<0.5) resulted in the target FAP ($<10\%$) for half of the on-source analyses. For the other half, a threshold on the initial magnitude (in the range 12–13 mag) was also required. For the whole-field analyses, an initial magnitude threshold of 14 mag was demanded for the TAROT follow-up of G19377 and a threshold of 10 mag for the Zadko follow-up of G19377, and the Zadko and TAROT follow-up of G20190. For these last three follow-ups the presence of observations taken months after the GW trigger allowed the additional requirement of the object's presence in the early observations and its absence in the reference ones.

For the QUEST on-source analysis, two methods were used to estimate the false positives. First, the background was evaluated directly in each on-source area. Due to the low statistics in these areas, a second estimate was also produced by rescaling the background event counts in the entire CCD to the on-source area. The target FAP (evaluated by both methods) was achieved for the majority of galaxies by demanding a magnitude variation larger than 0.5 between the first night and follow-up night observations, and an initial magnitude brighter than 17.5 for G20190, and 18.5 for G23004. For eight galaxies associated with G23004, stronger thresholds on the initial magnitude (between 15 and 18.2) were required.

Simulations have been performed for each set of images by using the exact thresholds applied for the analysis of the data associated with the GW trigger to prove the ability to detect likely EM counterparts (GRBs and kilonovae), and to evaluate the search sensitivity for the analysis procedure described above (see Section 6).

4.2. ROTSE Search

The ROTSE-III network consists of four robotic telescopes at various locations around the world. For each GW trigger in the autumn run, the telescopes repeatedly observed a single field. Each field was observed in a series of 30 exposures on the first night after the trigger time. Follow-up images were collected over the next 30 nights, with observations spaced an

average of every 2 nights. Each follow-up observation included 8 exposures, each 20 or 60 s.

We used the existing ROTSE pipeline to analyze the images taken with the network. Based on the ISIS package,[149] which uses a single convolution algorithm described in Alard & Lupton (1998) and Alard (2000), the ROTSE pipeline was adapted to use cross correlation to improve image subtraction results. The details of this method can be found in Yuan & Akerlof (2008). The pipeline was implemented for our analysis to require minimal user interaction and for large scale processing which enabled characterization of the background, as described in Nuttall et al. (2013).

The pipeline began by stacking images from the same night on top of one another to form a coadded image. `SExtractor` was used to produce a list of objects and their coordinates for each coadded image. These images were then subtracted from the coadded reference image, and several criteria were imposed on any objects found in the subtracted image. Selection criteria included requiring a full width at half-maximum consistent with a point source, seeking a minimum fractional flux variation between images and a signal-to-noise ratio (S/N) greater than some amount. The specific criteria depended on the location of the source in an image. For example, if a source matched a star or an unknown object a flux change of 60% was required, whereas if a source was within 20% of the semi-major axis length from the center of a galaxy, but not consistent with a core, only a 3% flux change was required. The result was several lists of candidates (one from each night), which we combined to produce a single list of unique candidates which appeared in the images, and generated light curves for all candidates.

The vast majority of these candidates were due to poor subtraction, with a fraction of real but uninteresting transients (such as variable stars or asteroids). In order to remove contaminants from the list of candidate transients, each object was subjected to a series of cuts. In order to be of interest, the transient must have appeared on more than one night, shown a sufficiently decaying light curve 48 hr after the trigger, and not have been coincident with a known variable source (from the SIMBAD catalog[150]) or with a minor planet (Minor Planet Checker[151]). These cuts proved efficient at rejecting the majority of the background. Candidates were then highlighted if they overlapped with known galaxies or if their light curves were consistent with a target theoretical light curve (Metzger et al. 2010; Kann et al. 2011, 2010). They were also assigned an ad hoc ranking statistic, R, defined as:

$$R \equiv \sum_i (18 - m_i)\Theta(18 - m_i) \times w_i \, . \tag{2}$$

Here $\Theta(x)$ is the step function, m_i is the background-subtracted magnitude of the transient in image i, and w_i is a weight factor defined by

$$w_i = \begin{cases} 1 & t_i - t_{\rm GW} < 1\ {\rm day} \\ \left(1 + \log_{10} \frac{t_i - t_{\rm GW}}{1\ {\rm day}}\right)^{-3} & t_i - t_{\rm GW} \geqslant 1\ {\rm day} \end{cases} \tag{3}$$

where $t_{\rm GW}$ is the time of the GW trigger, $t_{\rm i}$ is the time of image i. The ranking statistic was designed to prefer events which were bright within a day of the trigger time and which appear in multiple images.

The ROTSE FAR was investigated by processing sets of images for each of 100 random field locations selected from the ROTSE archive. Each set contained ∼240 images of the field from a month of nominally nightly observing. The FAP for each GW candidate was estimated by counting the number of transient objects visible in archived images with a similar cadence as the images collected for that GW candidate. The ranking statistic for each such transient object was calculated using Equation (2). These studies allowed us to set thresholds on the ranking statistic to keep the target light curves, while rejecting contaminants.

4.3. Catalog-based Search for Pi of the Sky

POTS has an unusually wide FOV of $20^\circ \times 20^\circ$, with a typical limiting magnitude of 11.5 for a 10 s exposure. This allowed the telescope to image a large part of the sky in response to one LIGO/Virgo trigger, over $40^\circ \times 40^\circ$ on most nights. We used the standard *POTS* pipeline to analyze the images taken by the telescope. A detailed description may be found in Malek et al. (2009) and Sokolowski (2008). The full analysis was carried out in two steps. First, in each image taken by the telescope, the Guide Star Catalog (Jenkner et al. 1990) was used to identify previously unknown sources. Second, POTS's nova recognition algorithm was applied to the list of unknown sources. To separate optical transients from contaminating sources, the algorithm utilized several types of vetoes, including checks on background saturation, nearby bright objects, satellite databases, and the Guided Star Catalog. Objects that passed the cuts were then visually inspected.

During the human inspection stage, every candidate that was not identified as a satellite or background fluctuation was checked against lists of known sources. First, we queried the POTS, INTA (Spain) site for observations made in 2011. Due to the long time (∼1 yr) between the autumn science run and observations from the INTA site, any objects observed by INTA were likely unrelated to the GW trigger.[152] Finally, objects were cross-correlated with the SIMBAD catalog, and sources that appeared nearer than 150″ to the position of any known star or infrared source were rejected.

4.4. SkyMapper Search

SkyMapper obtained two epochs of an eight image mosaic covering a total of ∼42 deg^2 in response to the 2010 September 16 trigger. An image subtraction technique was applied to identify possible transients. The SkyMapper images were reduced via the normal bias subtraction, overscan correction and flat fielding using a custom made Python-based pipeline. Thereafter, frames from the two epochs were aligned with the `WCSREMAP`[153] routine and subtracted with `HOTPANTS`[154] to create residuals images. `SExtractor` was used to identify sources with S/N greater than three. Then, a series of cuts was applied to the `SExtractor` output parameters to identify noise and bad subtractions. These included using the ellipticity parameter, photometry from different size apertures, and catalog matching of variable stars. In addition, a study of the point-spread function (PSF) of each object was performed on the subtracted images by fitting the detection with a two-dimensional Gaussian and comparing the fit parameters to the expected, known, PSF. The

[149] http://www2.iap.fr/users/alard/package.html
[150] http://simbad.u-strasbg.fr/simbad/
[151] http://scully.cfa.harvard.edu/cgi-bin/checkmp.cgi

[152] All Pi of the Sky telescopes have the same cameras, so data gathered is easily comparable.
[153] http://www.astro.washington.edu/users/becker/v2.0/c_software.html
[154] http://www.astro.washington.edu/users/becker/hotpants.html

remaining objects were then examined manually to verify they correspond to an object which was visible in the first epoch and not detectable/fainter in the second. The light curves were then measured using differential photometry with nearby stars.

4.5. PTF Search

The PTF accepted the trigger of 2010 September 26. Nine PTF fields, each covering 7.26 deg^2, were schedule automatically for observations, and they were observed beginning ≈6 hr after the trigger time (since the trigger occurred during day-time on the Pacific Coast). PTF then repeated the observations on several subsequent nights. The number of follow-up observations was mainly limited by full moon constraints.

The imaged fields were searched for candidate transients using the image subtraction pipeline hosted at LBNL (P. E. Nugent et al. 2014, in preparation; Gal-Yam et al. 2011). Only three of the fields imaged by PTF had previously constructed reference images. For the rest of the fields, image subtraction was performed using a reference image constructed by co-adding several images taken during the first night of observations. Image differencing inherently produces a large number of spurious candidates, and only a small fraction (less than few percent) of these are real events. As described in Bloom et al. (2012), in a typical PTF night of order 10^5 residual sources are found per 100–200 deg^2 of imaging, after performing subtraction of the reference image.

To distinguish between astrophysical objects and "bogus" image subtraction residuals, we made use of a classification parameter named the "realbogus" parameter (*RB*; Bloom et al. 2012), which was assigned by a machine-learned (ML) classifier so as to reasonably mimic the human scanning decision of real or bogus. The *RB* parameter ranged from 0 (definitely bogus) to 1 (definitely real), and was constructed from 28 `SExtractor` output parameters, including magnitude, ellipticity of the source, and distance from the candidate to reference source.

To maximize the chances of identifying a potential optical counterpart to G21852, the images collected by PTF were analyzed using two different procedures for transient identification, both based on the *RB* parameter as a starting point (P. E. Nugent et al. 2014, in preparation). While the first procedure (hereafter, the "automated" approach) was largely based on automated ML techniques and optimized for fast transients, the second (hereafter, the "citizen-based" approach) was largely based on a citizen project (Smith et al. 2011) and optimized for supernova searches. In what follows, we describe these two approaches in more detail.

4.5.1. Automated Approach

We identified the most promising fast transient candidates (i.e., transients with a variability on a timescale of a week or less) obtained in an image subtraction by applying the following selection criteria:

1. $RB \geqslant 0.17$ in at least one detection;
2. matching of the candidate with at least one other detection with $RB \geqslant 0.07$;
3. the second detection should be coincident with the candidate position within 2″ on the sky;
4. the second detection should be at least 45 minutes (and no more than 6 days) before or after the original candidate.

Candidates satisfying the above criteria were further passed through the so-called "Oarical classification routine" which, as part of the standard PTF operations, was designed to distinguish between two main classes of events, namely "transients" and "variable stars." The classifier used both time-domain features, such as light-curve evolution, and context features, including the location of the source relative to known stars and galaxies (see Bloom et al. 2012 for details).

Candidates with high *RB* and high classification confidence were saved automatically in the so-called "PTF Marshal" web archive, and thus assigned an official "PTF name" and a tentative object type. Further spectroscopic follow-up was pursued only for sources that looked particularly promising in relation with the main science objectives of the PTF survey.

The main challenge of our study was to identify, among the list of candidates retrieved using the criteria described here (and in the absence of spectral classification for most of them), the ones more likely to be of interest for LIGO and Virgo, in the sense of having properties consistent with "explosive" events such as binary mergers or stellar collapses, that our search was targeting.

4.5.2. Citizen-based Approach

In addition to the list of candidates described in the previous section, we also considered candidates passing selection criteria optimized for the identification of young supernovae:

1. candidate *RB* parameter value >0.07;
2. detected at least twice;
3. flat or rising light curve;
4. not seen prior to 10 days before the earliest day.

As part of normal PTF operations during 2010, candidates passing the above criteria were further examined by citizen scientists through the Galaxy Zoo Supernovae project (Smith et al. 2011). The Galaxy Zoo scanners were presented with a series of detection "triplets" for each candidate. Each triplet contained three images: the current image of the field containing the candidate; the historical or reference image of the same field; and the image of the difference between the previous two (which should contain only the candidate light). Each examiner was asked a series of questions to determine if the candidate appeared consistent with a supernova, and the answers were converted into a score. The arithmetic mean of the scores from many scanners was calculated, and candidates with strong (supernova-like) scores were counted in our final list of candidates.

4.5.3. Selection for LIGO/Virgo Event Candidates

All of the candidates from both the automated approach and citizen-based approach were vetted by human scanners to judge which candidates deserved to be kept for further investigation as "LIGO/Virgo interesting." To do so, we took advantage of two new parameters recently developed by the PTF team, to improve confidence in transient identification. The first parameter is the so-called "realbogus 2" (*RB2*; Brink et al. 2013). The *RB2* parameter is similar to the *RB* parameter, but it was defined by using a much larger training sample (78,000 objects). The *RB2* also utilized some additional features that the original *RB* parameter did not use, including correlations in different PTF filters. By using a sample of spectroscopically confirmed sources discovered by PTF, it has been found that selecting candidates with $RB2 > 0.3$ yields a false positive rate of ≈3%, and a missed detection rate of ≈3.2% (Brink et al. 2013).

The second parameter is known as the *Supernova Zoo predictor*, a ML classifier that was trained using the Supernova Zoo mark up of tens of thousands of candidate transients, so as to construct a classifier capable of efficiently discovering

supernovae. The Supernova Zoo predictor assigns a score (hereafter, SN_{zoo}) to each of the candidates, which is higher for more promising candidates (i.e., the ones that are most likely to be real supernovae). By using a sample of spectroscopically confirmed supernovae discovered by PTF, it has been found that selecting candidates with $SN_{zoo} > 0.025$ yields a false positive rate of ≈14%, and a missed detection rate of ≈10%.

For our final selection cuts, we applied the following criteria:

1. Was the transient classified spectroscopically as a variable star, an AGN, or a SN of type Ia? If yes, discard.
2. Was the candidate detected for the first time before the GW trigger time? If yes, discard.
3. Does the transient appear to have subtracted correctly? If not, discard after double checking that this is consistent with a low value of the *RB2* ($RB2 < 0.3$) *and* of the supernova zoo predictor parameter ($SN_{zoo} < 0.025$).
4. Is the candidate classified as a STAR in Sloan Digital Sky Survey (SDSS), and/or is it spatially coincident with a known stellar or AGN source in SIMBAD? If yes, discard.
5. If the analyzed field is not in the SDSS footprint and nothing is found in SIMBAD (see above), can the candidate be securely associated with a point-like host in the PTF reference image (or in an image taken a year after the LIGO/Virgo trigger in case a previous reference image was not available)? If yes, is the Oarical classification (see Section 4.5) consistent with a "variable star" and/or is there enough photometry to confirm a long-term variable origin from the light curve? If yes, discard.
6. If the analyzed field is not in the SDSS footprint, nothing is found in SIMBAD, and a point-like host cannot be identified in the reference image (see above), then: Does the candidate have *both RB2* and SN_{zoo} below threshold? Or, is it classified by the Oarical classifier (Section 4.5) as variable star or AGN, and is there enough photometry to confirm a long-term variable origin from the light curve? If yes, discard.

4.6. Liverpool Telescope Search

The Liverpool Telescope observed the G23004 trigger using both the 4.6 arcmin FOV RATCam instrument and the 1° FOV SkyCamZ camera. This produced a total of 22 SDSS r'-band RATCam images and 121 "clear" filter SkyCamZ images from two nights 29 days apart. In addition, 3 RATCam and 17 SkyCamZ images were taken in early 2012 to serve as reference images for image subtraction. The analysis made use of several freely available software packages, and was split into several sections written in Python.

First, we combined the images from 2012 to create our reference images. This was done by aligning the images using the `WCSRemap`[155] package and combining them using the `SWarp`[156] package. We also combined sets of five SkyCamZ images on each night to improve image quality and provide a similar cadence to the RATCam images. We removed one RATCam image and two SkyCamZ images due to quality issues.

Second, as the SkyCamZ images used a non-standard filter,[157] they were calibrated using the USNO-B catalog of stars to determine the zero point offset required to calculate correct magnitudes, in the same way ROTSE and TAROT images were calibrated (see Section 4.1). This was done by comparing the USNO-B *R*-band magnitude of stars in the combined SkyCamZ fields with those same stars found using `SExtractor`.

The images were then aligned individually to the reference images, again using `WCSRemap`, and the reference image was subtracted using the `HOTPANTS`[158] image subtraction package. `SExtractor` was then used to detect potential candidates in each individual field with a minimum of 4 pixels each with a flux greater than 4σ above the background noise of the image. This reduced the frequency of detecting uninteresting objects, such as cosmic rays, extremely faint stars and noise from the image subtraction process while allowing us to achieve a sensitivity around 20th magnitude in the narrow-field RATCam images.

Using the output of `SExtractor` from each of the subtracted images, a Python script combined the objects found into a master list containing every unique candidate found in those images, along with useful parameters from `SExtractor`. From this data, a series of cuts were made to find candidates interesting to this analysis. First, candidates found to be near an image edge (or a bad pixel strip in the case of RATCam images) were rejected. Second, a cut was made to remove artifacts due to bad subtraction. This was achieved by examining the region in the subtracted image around the candidate and calculating the total flux more than 4σ below the median noise of the image. Since bad subtractions are usually caused by poor alignment or convolution, they typically produce a large amount of "negative" flux in the residual image. If the total amount of flux below this threshold was the equivalent required for detection of candidates (4 pixels above 4σ) then the candidate was rejected. The next cut removed candidates not seen in at least half of the images available on the first night, to ensure candidates were visible long enough to be used in our analysis. We also rejected candidates that appeared close to known variable stars and minor planets. Finally, we required that a candidate must decrease in brightness by more than 5σ of the median error on the magnitude measurements from `SExtractor`, from the first night to the second night 29 days later. Since the pipeline is designed to work with images from two telescopes for this analysis which may have different magnitude errors for the same trigger, we used a threshold based on the noise in the image rather than a fixed magnitude variation in the same way as ROTSE and TAROT.

Any objects that remained after these cuts were considered likely candidates, and looked at in more detail. This was done by plotting the light curves of each object across both nights and inspecting images of the candidates in both the original and subtracted images. This allowed us to gauge whether any transients warranted further investigation.

5. OPTICAL TRANSIENT SEARCH RESULTS

In this section we present the details of the associated optical images for each GW trigger. The center location of each observed field is shown in Table 5. We also present the results of the transient analysis for each data set. Data from the two periods of our search were handled differently. The winter run triggers were not observed with sufficient cadence to reconstruct light curves, so only a limited analysis was performed on those triggers. Section 5.1 describes the results of the analysis along with figures showing the position reconstruction and image locations for each winter run GW trigger (Figures 2 and 3).

[155] http://www.astro.washington.edu/users/becker/v2.0/c_software.html
[156] http://www.astromatic.net/software/swarp
[157] http://telescope.livjm.ac.uk/Info/TelInst/Inst/SkyCam/
[158] http://www.astro.washington.edu/users/becker/hotpants.html

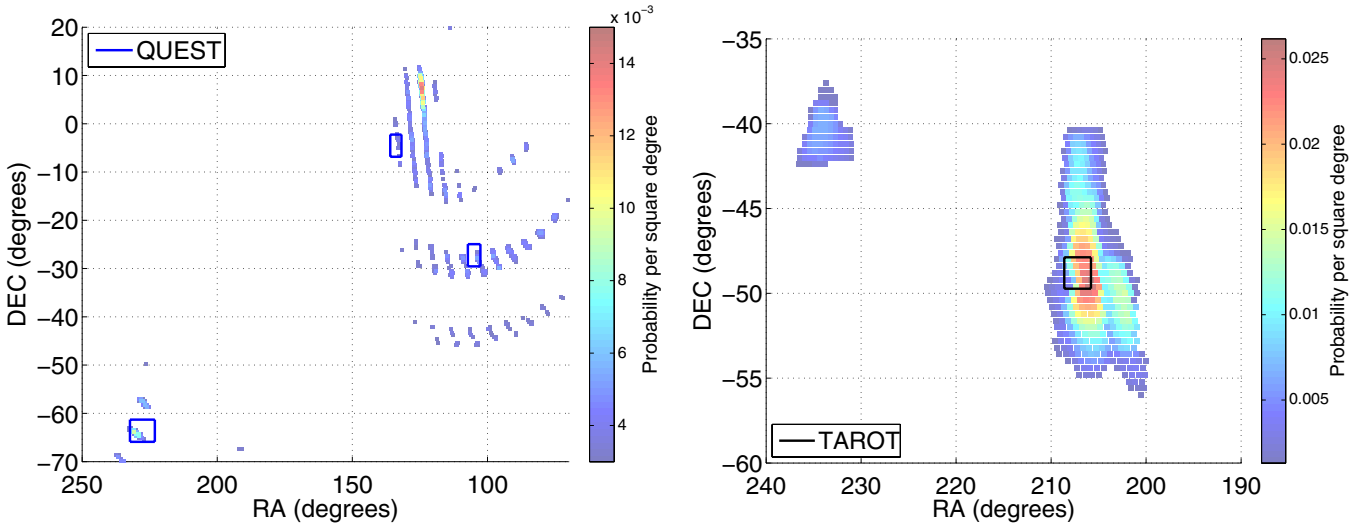

Figure 2. GW skymaps for triggers G3821 (left) and CWB1 (right). The colored regions show the estimated probability per square degree that each location is the true source direction before applying the galaxy weighting. The locations of the observed fields (selected using galaxy weighting) for telescopes that observed the trigger are also marked.

(A color version of this figure is available in the online journal.)

Table 5
Center Locations of All Fields Observed

GW Trigger	Telescope	R.A.	Decl.	R.A.	Decl.	R.A.	Decl.
G3821	QUEST	104.89	−27.94	133.88	−5.24	227.61	−64.26
CWB1	TAROT	207.21	−48.80				
G4202	QUEST	89.34	−0.70	86.33	−9.78	89.34	−5.24
CWB2	QUEST	81.00	−32.49	75.63	−50.65	91.23	−41.57
G19377	ROTSE-c	115.56	−30.00				
	SkyMapper	115.43	−30.03	120.01	−29.91	110.78	−29.92
		115.40	−34.00	115.39	−25.99	110.94	−25.93
		110.58	−33.91	120.22	−33.90		
	TAROT	115.40	−30.00				
	Zadko	110.98	−27.53	114.75	−22.05	115.25	−32.07
		115.80	−29.98	115.85	−29.22		
G20190	ROTSE-abcd	333.25	18.03				
	TAROT	333.33	18.00				
	Zadko	322.49	12.17	323.37	−0.82	329.77	18.18
		330.17	17.74	333.96	19.23		
	QUEST	336.29	8.50	334.49	10.63	331.61	17.57
G21852	ROTSE-b	11.04	41.61				
	PTF	11.39	41.62	55.80	−19.12	52.20	−19.12
		56.93	−21.37	39.42	−7.87	52.25	−28.12
		55.24	−16.87	51.15	−25.87	34.38	−32.62
G23004	ROTSE-bcd	61.97	−20.91				
	Liverpool	61.11	−2.20				
	Pi of the Sky	Various					

Note. All coordinates are in degrees using the J2000 equinox.

The methods described in Section 4 were applied to the data collected in response to each GW trigger in the autumn run. To display the sky coverage and depth of each response, two panels are presented for each autumn run trigger (Figures 4–7). The left panel shows the GW skymap (without the use of galaxy weighting) along with the positions and approximate field sizes of each observed tile. The right panel shows a timeline of the observations by each observatory. The *y*-axes of the timeline plots display the limiting magnitudes of the observations. In these plots, for TAROT, POTS, and Zadko, each arrow represents one observation. For QUEST, each arrow is a median of limiting magnitudes over the CCDs covering the on-source galaxy regions observed at a given time. For PTF, the arrows give the limiting magnitudes reached in a central CCD of the camera, for the field containing the M31 galaxy (which was observed with highest cadence).

The right panel of each figure also shows several models for possible EM counterparts. The off-axis long GRB model (L-GRB; solid dark green line) is from van Eerten et al. (2010), and assumes a total energy in the jets of 2×10^{51} erg, jet half opening angle of 0.2 rad, off-axis observer's angle of 0.3 rad, interstellar medium number density of 1 cm^{-3}, and distance of 30 Mpc. We note that within this model, the associated optical transient peaks at ≈1 day since trigger. The off-axis

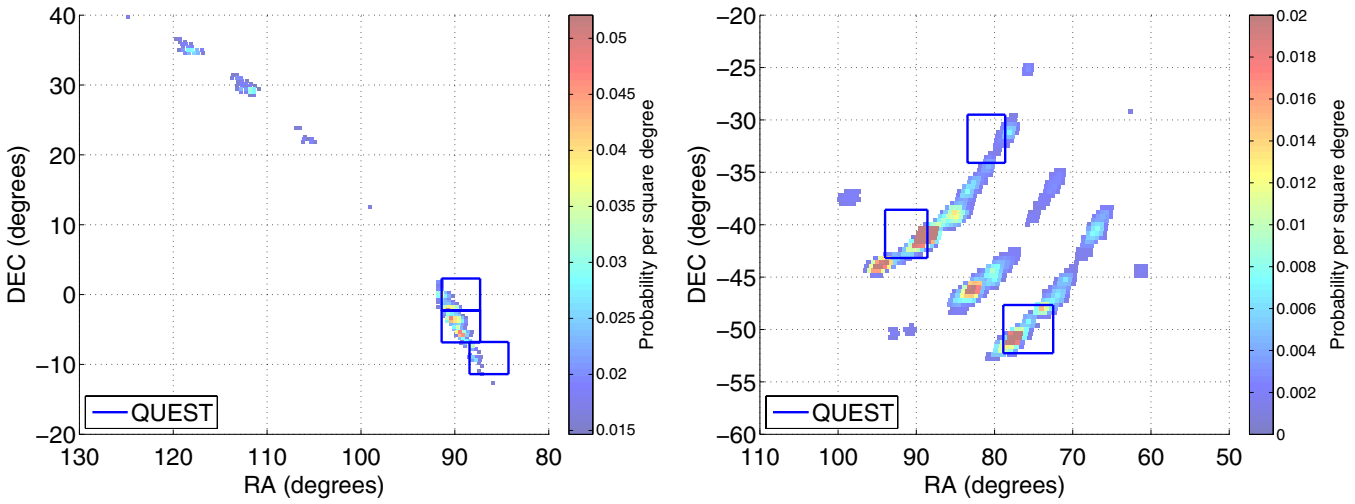

Figure 3. GW skymaps for triggers G4202 (left) and CWB2 (right). See Figure 2 caption for explanation.
(A color version of this figure is available in the online journal.)

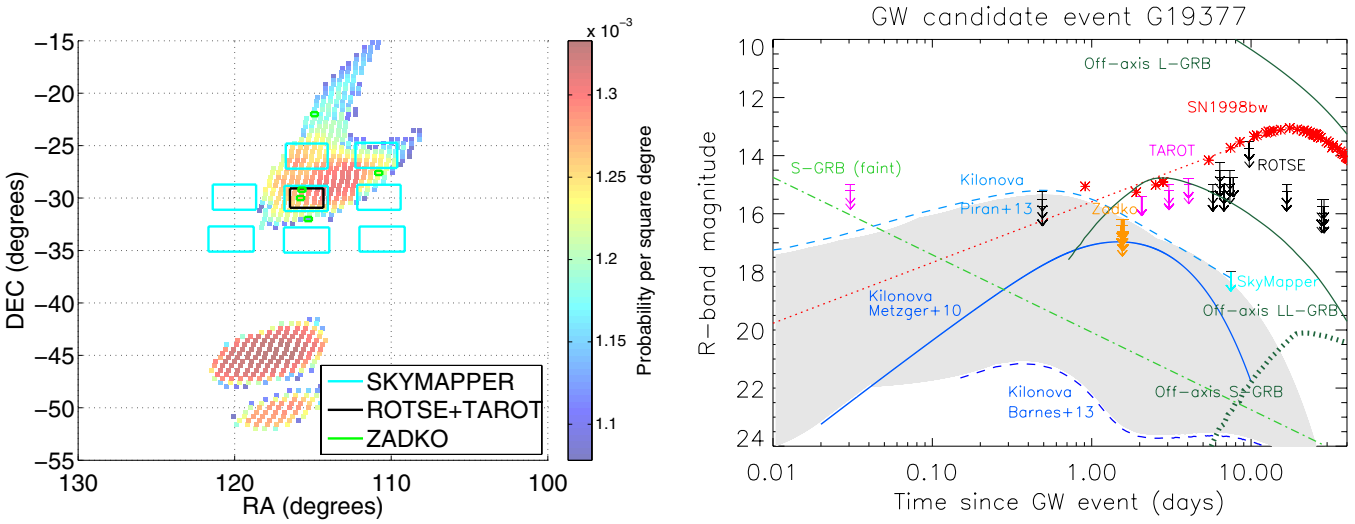

Figure 4. On the left, the GW skymap for G19377, which was later revealed to be a blind injection. The skymap shows the probability per square degree that each location is the true source direction before applying the galaxy weighting. The locations of the observed fields (selected using galaxy weighting) for telescopes that observed the trigger are also marked. On the right, a timeline showing when each telescope observed the requested fields, with time zero corresponding to the GW trigger time. Model light curves for several sources, scaled to 30 Mpc, are shown for comparison (see Section 5 for details).
(A color version of this figure is available in the online journal.)

low-luminosity GRB model (LL-GRB; dash-dot-dot-dotted dark green line) is from van Eerten & MacFadyen (2011), and assumes a total energy in the jets of 10^{50} erg, jet half opening angle of 0.2 rad, off-axis observer's angle of 0.4 rad, and interstellar medium density of 1 cm^{-3}. The off-axis short GRB model (S-GRB; dashed dark green line) also refers to a total energy in the jets of 10^{50} erg (and similar jet and observer's angles), but the interstellar medium density is set to 10^{-3} cm^{-3}. The light green line represents the case of a faint short GRB observed on-axis (see Table 1 and Kann et al. 2010, 2011). The emission from typical short GRBs and long GRBs observed on-axis lies above this line. In particular, on-axis long GRBs at 30 Mpc would appear as very bright optical transients.

The kilonova models are courtesy of Barnes & Kasen (dashed dark blue), B. Metzger (dark blue), and E. Nakar (light blue). Specifically, the light blue line represents one of the kilonova bolometric light curves from Piran et al. (2013) (BH–NS merger with BH mass of 10 $M_\odot$). This light curve assumes that all of the bolometric luminosity is emitted in the R-band, and it represents an upper-limit to the true R-band luminosity of the kilonova event. The solid dark blue line is one of the kilonova light curves from Metzger et al. (2010), and is calculated for an ejecta mass $10^{-2}\,M_\odot$ assuming a blackbody emission. Finally, the dashed dark blue line is one of the kilonova models from Barnes & Kasen (2013), for the case of low-velocity ($0.1c$) low-mass ($M = 10^{-3}\,M_\odot$) ejecta. Since the kilonova models are subject to large uncertainties, we selected these three light curves to give an indication of the possible scatter in the model predictions.

Finally, the prototype emission from a GRB-associated SN is plotted with a red dotted line: this is a tentative extrapolation to early times of the R-band light curve observed for SN 1998bw (red asterisks; Clocchiatti et al. 2011), associated with GRB 980425 (Galama et al. 1998). The light curve assumes that SN 1998bw exploded at the same time at which GRB 980425 was triggered.

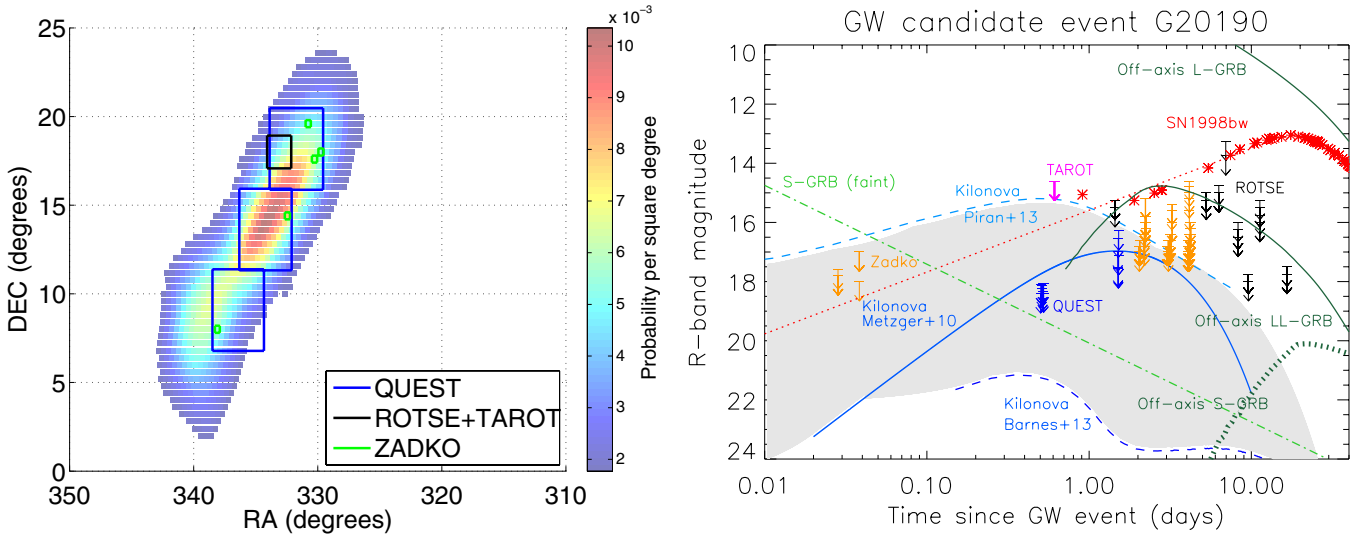

Figure 5. GW skymap and observations of trigger G20190. See Figure 4 caption for explanation.
(A color version of this figure is available in the online journal.)

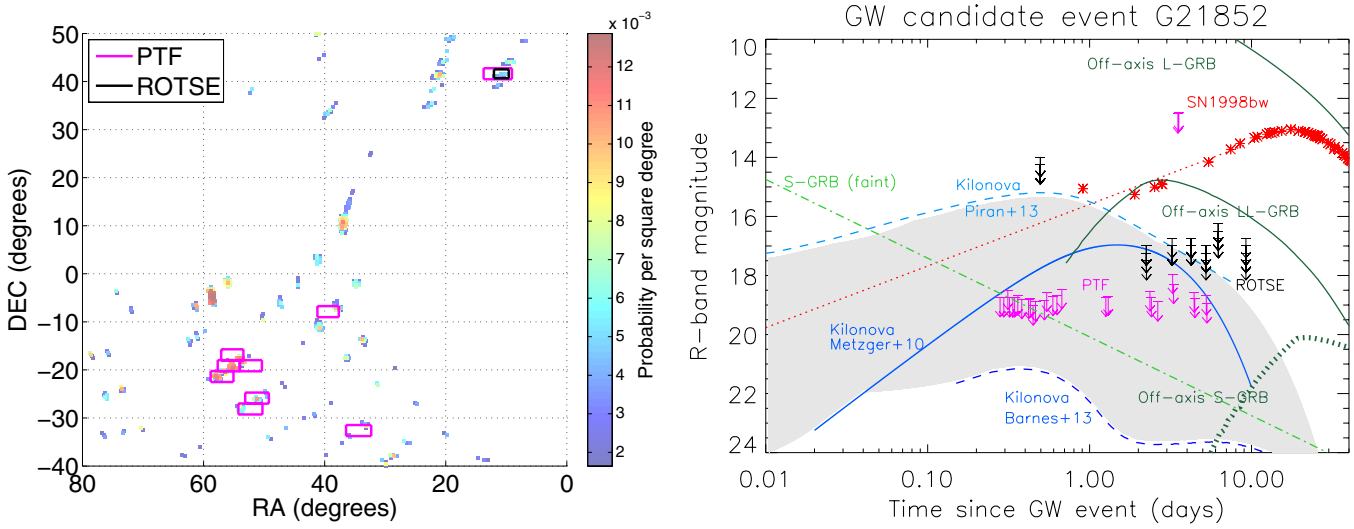

Figure 6. GW skymap and observations of trigger G21852. See Figure 4 caption for explanation.
(A color version of this figure is available in the online journal.)

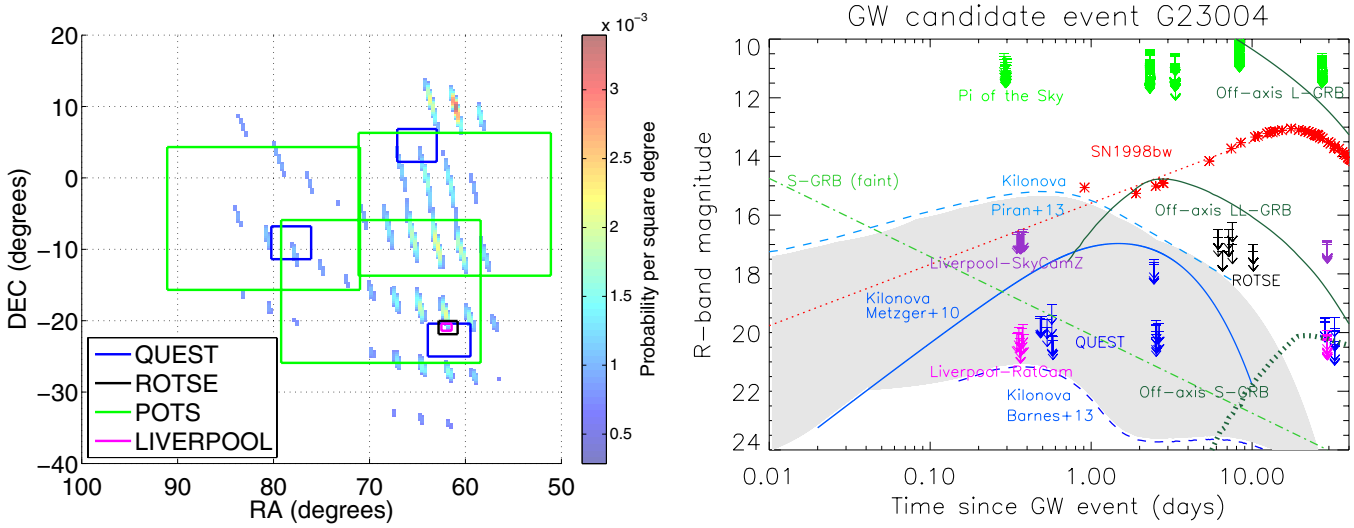

Figure 7. GW skymap and observations of trigger G23004. See Figure 4 caption for explanation. The shown Pi of the Sky (POTS) fields are a subset of the 10 overlapping pointing positions used to observe the GW uncertainty region.
(A color version of this figure is available in the online journal.)

5.1. Winter Run Triggers

For each winter run trigger, images were collected only during one night. The absence of a second night's observations prevented the construction of variability measures and limited the analyses to only identify "unknown objects," i.e., those not listed in the USNO catalog or with a magnitude significantly different from USNO, but visible in all the collected images. For both the TAROT and QUEST image analysis procedure, at least one observation on another night would have been required to identify a unique electromagnetic counterpart.

In the winter run, TAROT responded to one trigger, CWB1, and collected six images starting the single night observation at T+3d11h. The QUEST camera responded to three triggers, G3821, G4202, CWB2, starting the observations at T+9h46m, T+24m, and T+16h12m, respectively. For each trigger it collected images corresponding to three fields. Each field was observed twice within 20 minutes during the same night.

The TAROT observation associated with CWB1 reached a sensitivity of 15.8 mag. Fifteen galaxies with a distance smaller than 50 Mpc were in the FOV. The analysis found 9 unknown objects in the on-source region and 46 in the entire FOV up to the limiting magnitude. No unknown objects were found with magnitude brighter than 11.8 in the on-source region and brighter than 10.7 mag in the entire FOV.

The three QUEST fields associated with G3821 included a total of 34 galaxies with a distance smaller than 50 Mpc. Only 14 of the galaxies were analyzed due to the exclusion of galaxies observed only one time or lying in CCDs that did not work or had calibration problems. The average limiting magnitude was about 18.6 mag.

For trigger G4202 the three fields included a total of 17 galaxies with a distance smaller than 50 Mpc. Ten galaxies were removed from the analysis because they were observed only one time or associated with poor image quality (impacted by bad lines and pixels or by background subtraction artifacts) or calibration problems of the CCDs (astrometric calibration or flat-field problems). An average limiting magnitude of 19.2 mag was reached during the observations.

For trigger CWB2 the three fields included a total of 12 galaxies with a distance smaller than 50 Mpc. Two of the galaxies were not analyzed due to poor image quality or CCD calibration problems. An average limiting magnitude of 19.8 mag was reached during the observations.

The QUEST analysis found 9, 1 and 1 unknown objects in the on-source region with a magnitude brighter than 14 mag for the triggers G3821, G4202 and CWB2, respectively. The number of unknown objects increased to 140, 35, 6 for magnitudes brighter than 18 mag. The number of unknown objects showed a stronger dependence on the density of image artifacts and stars in the FOV than on the on-source area. No "unknown objects" were found for magnitude brighter than 9, 12, 7 mag for G3821, G4202 and CWB2, respectively.

5.2. G19377

Event G19377 was a simulated signal added to the GW detector data in order to test our data analysis pipelines. The ROTSE-IIIc telescope responded at T+$\sim$12 hr when 30, 20 s exposure images were taken within $\sim$15 minutes. On subsequent follow-up nights (6–29) both ROTSE-IIIa and c telescopes gathered 80, 20 s exposure images. The images from the two scopes varied vastly in terms of image quality, which posed difficulties for injection studies. We discarded the lower quality images from the 3c telescope, leaving just the 3a images, with an average limiting magnitude of 15.1. Two galaxies at $\sim$24 Mpc (PGC 078144 and PGC 078133) were visible within the FOV. The ROTSE image processing pipeline revealed 68 unique objects, one of which passed the candidate validation. Further tests found this candidate was consistent with background, with a FAP of 7%. This left no significant candidates. At the location of this background transient there is a known star (red magnitude of 13.1 from the USNO catalog), which shows no significant magnitude variation in the TAROT images associated with the same GW trigger. This location was not covered by the *Swift* observations taken for G19377. We also tried analyzing images from both the 3a and 3c telescopes together, and found no additional candidates.

SkyMapper observed an eight tile mosaic, 7 days after the initial alert. An analysis was performed, but no plausible transients were discovered.

TAROT took images starting at T+43m and repeated the observations at T+2d, T+3d and T+4d. Observations from the four nights displayed an average limiting magnitude of 15.1. The on-source analysis was performed on the two same galaxies observed by ROTSE and identified no transient counterpart. The whole-field analysis was performed with an initial magnitude threshold of 14 mag, and identified one transient candidate with a slope index of 0.6. A deeper analysis showed that this candidate resulted from an artifact of the de-blending in crowded images.

The Zadko telescope observed the regions around the five galaxies evaluated to be the most likely hosts of the G19377 trigger: NGC 2380, ESO 560-004, ESO 429-012, PGC 078133, and PGC 078144; the last two being in common with ROTSE and TAROT. The observations started at T+1d12.6h and were repeated 5 months later for reference. The average limiting magnitude for both the early and reference images was 16.5 mag. No electromagnetic counterparts were identified by either the on-source on whole-field analysis.

5.3. G20190

All four ROTSE-III telescopes responded to this GW trigger, taking images spanning T+34h38m to T+29d, centered on the region around the galaxy UGC 11944. However, all images taken with the ROTSE-IIIa, b and d telescopes were discarded because of defocusing factors in addition to weather conditions at those sites being less than optimal. This resulted in 56 images being used for the analysis, with an average limiting magnitude of 15.5. The ROTSE image subtraction pipeline found 77 potential candidates, none of which passed the candidate validation procedure.

The TAROT telescope collected three images in association with G20190. Due to the full moon only an average limiting magnitude of 14.6 mag was reached. Nine months later 18 images were taken by TAROT in the same region of the sky as reference. A mean limiting magnitude of 17 mag was reached during this second observation. No counterpart with a FAP less than 10% was identified by the on-source analysis. The whole-field analysis was performed with a threshold of 10 mag on the initial magnitude and the required presence in the first three images and absence in the reference images. It resulted in four identified candidates. The candidates were seen to be image artifacts linked to the spikes of saturated stars.

The Zadko telescope was pointed toward two Galactic globular clusters: NGC 7078 and NGC 7089, and three galaxies UGC 11868, NGC 7177, and NGC 7241, evaluated to be the most likely hosts of the GW source. Observations of galaxies UGC

11868 and NGC 7241 were taken about 50 minutes after the GW trigger. All five fields were observed subsequently during at least two nights between T+1d and T+4d. The observations were repeated 11 months later for reference. The average limiting magnitudes were 16.4 mag and 17.3 mag for the very first and reference observations, respectively. The on-source analysis identified three transient candidates associated with NGC 7078 and 15 associated with the center of NGC 7089. The candidates were found to be due to problematic de-blending in the central region of globular clusters. No transient was identified by the on-source analysis associated with the three galaxies. The whole-field analysis required a magnitude brighter than 10 and the presence during the first nights and absence in the reference images. This resulted in no detected transient.

The QUEST observations started at T+12h3m. Each field was observed twice within 15 minutes as pairs of images dithered to fill the gaps between rows of CCDs. The entire observation sequence was repeated at T+1.5d. A total of 10 galaxies with a distance smaller than 30 Mpc were identified in the three fields. Three of the galaxies were not analyzed due to poor image quality CCDs or calibration problems. The observation was taken during a full moon night that allowed an average limiting magnitude of 17.6 mag. The on-source analysis[159] identified one possible transient with a FAP less than 10% (see Section 6) associated with the galaxy UGC 11916. A deeper analysis of the candidate showed this to be artificial. The analysis pipeline identified the possible GW host galaxy itself as a transient due to variations in the estimate of its surface photometry over the two nights. An estimate using fixed photometry apertures indicated magnitudes in agreement within the errors with no flux decrease.

5.4. G21852

ROTSE-IIIb took images spanning T+11h53m to T+29d centered on a region containing both M31 and M110. One follow-up night had to be ignored due to defocusing issues. The average limiting magnitude of the images was 16.6, with 81% of them having an exposure times of 60s. The subtraction pipeline found 187 objects, which resulted in four candidates after candidate validation. All four candidates overlapped with one of the galaxies mentioned, however all were consistent with background. The highest ranked candidate had a FAP of 9%. Consequently, we found no significant candidates. Within the 2 arcsec positional accuracy of PTF, the ROTSE background events are all coincident with known stars, and according to the PTF analysis criteria applied, these sources are not considered candidates.

PTF observed nine different fields on five nights, beginning at T+6h37m. The median limiting magnitude reached in the observed fields over the observation time (and over the 11 CCDs that make the core of the PTF imager) was in the range $R \approx 20.2$–19.2. The images collected by PTF were analyzed using two different procedures for transient identification, one entirely based on automated selection criteria for fast transients, and the other largely based on a citizen project targeting supernovae (see Section 4.5 for more details). These procedures for transient identification were routinely used by the PTF survey (P. E. Nugent et al. 2014, in preparation). By applying the selection criteria for fast transients (automated approach; see Section 4.5.1) on the images that were taken for follow-up of trigger G21852, we obtained a list of 172 candidates, none of which passed the vetting for "LIGO/Virgo interesting" transients performed according to the criteria described in Section 4.5.3. We also applied these last criteria to the candidates obtained via the citizen-based approach (optimized for supernova searches—see Section 4.5.2). Of the 218 candidates selected according to criteria (1)–(4) in Section 4.5.2 and sent out to the citizens for scanning, 28 were saved by the citizens and assigned an official PTF name. However, none of these 28 candidates passed the additional vetting described in Section 4.5.3. We also took a closer look at 55 other candidates that were not saved by the citizens, but that had a SN_{zoo} predictor score >0.025 *or* a *RB2* > 0.3 (see Section 4.5.3). We vetted these candidates according to criteria (1)–(5) in Section 4.5.3, and none of them passed our screening.

[159] The 7% of the total on-source area within the gaps between the CCDs does not have data and was not analyzed.

5.5. G23004

The ROTSE-IIIb, c and d telescopes responded to G23004 at T+6h25m and collected data up to T+29d. These images contained one galaxy (NGC 1518) at 11.5 Mpc within the FOV. Around 75% of the data was of poor quality; many of the images were out of focus and cloud cover was also a factor. This resulted in the analysis of 30 images with an average limiting magnitude of 16.7. The ROTSE subtraction pipeline found 124 potential candidates of which none survived the candidate validation tests.

The Liverpool Telescope observed a single field centered on the location of the galaxy NGC 1507, with one hour of observations taken at T+9h and a further one hour at T+30d. The limiting magnitude of the RATCam images was $r' \approx 20.5$, averaged over all images, with the calibrated limiting magnitude of the SkyCamZ images averaging $R \approx 17.5$. We found 406 unique objects in the RATCam images and 163 unique objects in the SkyCamZ images. After applying cuts described in Section 4 we found no candidates in either the RATCam or SkyCamZ images that met our criteria.

The POTS telescope responded at T+6h56m after the alert. On the first night the telescope used 10 different pointing locations to cover an area containing 40% of the G23004 probability map. Each location was imaged twice. The limiting magnitudes for the first night's observations spanned 10.5–11.0 mag. On the first night there were over 700 cases that were recognized by the pipeline as possible optical transients, but all of them were either already included in the database of weak stars or were noise due to ice crystals on the camera. There were no real optical transients found. The same fields were followed up on the nights of October 5, 6, 7, 11, and 30. Each follow-up night's observed area was covered by nine pointing locations, with each location imaged at least three times. Images from the first four nights were searched by the pipeline for optical transients, and 40 objects were identified as existing in images over multiple nights and have been present on all frames that were taken of that field. Each of these was manually investigated, and none were found to be linked to the GW trigger. Most of the 40 objects were traced to variable stars or were caused by ice crystals on the camera.

The QUEST follow-up for this GW trigger consisted of three nights of observations over three different fields. The first observation began at T+11h32m and then observations were repeated at T+2.4d and T+32.4d. Each night's observations included two visits to each of two dithered positions for each of the three field locations. A total of 32 galaxies with a distance smaller than 50 Mpc were identified in the three fields. Due to inoperative CCDs or CCD calibration problems the regions occupied by four galaxies were not analyzed. The average limiting

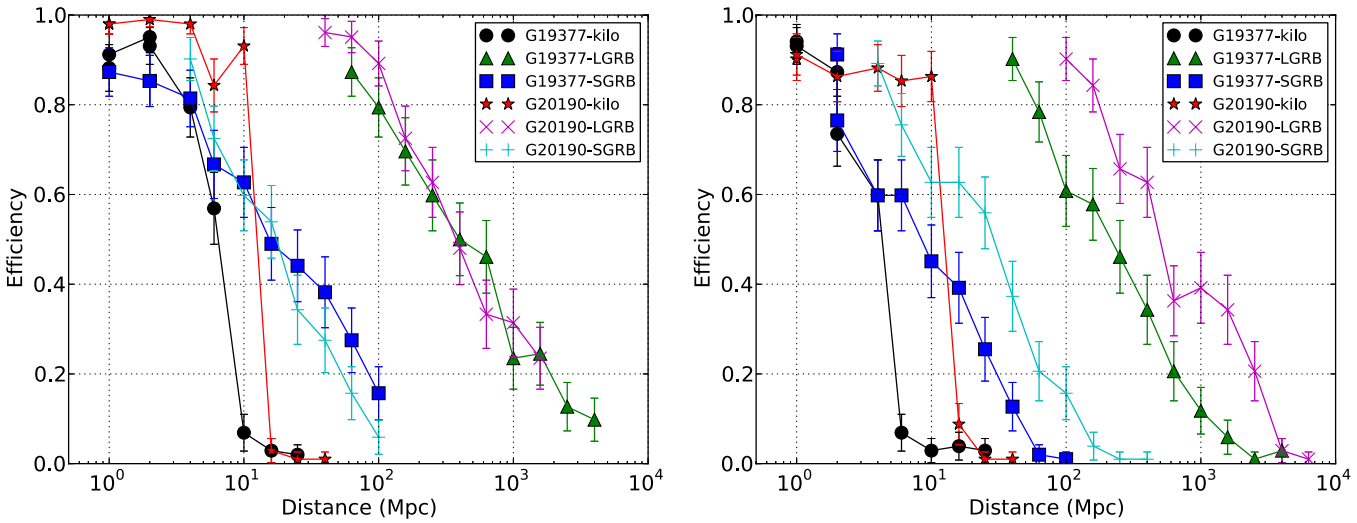

Figure 8. Efficiency in recovering simulated optical transients in the TAROT data (left) and Zadko data (right). The figure reflects the success rate in recovering transients added to the observed fields, and does not include efficiency lost due to observing only a fraction of the possible source locations. The signals have been simulated based on the models shown in Table 1, with the power law flux of each GRB randomly scaled within the shown range of normalization conditions.

(A color version of this figure is available in the online journal.)

magnitude for the three night observations was 19.7 mag. The *on-source*[160] analysis identified one possible transient with an "on source" FAP of less than 10% (see Section 6). The candidate transient overlaid the extended emission of the galaxy IC0402. A deeper analysis indicated no flux change for the object: the point source immersed in the fainter galaxy edge emission has a similar neighboring object that biased its photometry. Using a suitable fixed photometry aperture the magnitudes of the object agree within the errors in all the images. The object could be a foreground star not listed in the USNO catalog or a bright knot of one of the galaxy's arms.

6. EFFICIENCIES FOR RECOVERING SIMULATED OPTICAL TRANSIENTS

Simulated transients were added to each set of images to measure the efficiency in recovering optical counterparts located at different distances from earth. The different telescope pipelines were run over the simulated data with the same analysis tuning used in the real data. For TAROT, Zadko, QUEST, ROTSE, and the Liverpool Telescope the simulated transients reproduced the observed light curves (see, e.g., Figures 5 and 4 of Kann et al. 2011, 2010) of on-axis GRB afterglows and a modeled light curve for the kilonovae (Metzger et al. 2010; Piran et al. 2013). Table 1 summarizes the features of injected models. These models were scaled on the basis of the observation time from the GW trigger and the source distance. We emphasize here that while the simulated GRB afterglows cover the range of observed luminosities, kilonovae have not been observed yet and so our efficiency results are dependent on the assumed model.

6.1. TAROT and Zadko Telescope

For each set of images collected by TAROT and the Zadko telescopes, 100 simulated transients were added to the data for each counterpart model and distance. To model PSF variations in the wide-field images, reference model stars were identified in each image, and the PSF of the reference star closest to the injection position was used for each simulated object. For the GRB afterglows, we used a range of magnitudes uniformly distributed between the brightest and faintest GRBs (see normalization in Table 1). The results are presented in Figure 8. Long GRB afterglows/short GRB afterglows/kilonovae were recovered with 50% efficiency in TAROT observations to distances of 400 Mpc/18 Mpc/6.5 Mpc respectively for trigger G19377 and 355 Mpc/16 Mpc/13 Mpc for trigger G20190. For Zadko Telescope observations, we obtained 195 Mpc/8 Mpc/4 Mpc for G19377, and 505 Mpc/ 25 Mpc 13 Mpc for G20190. As expected, the results showed some dependence on the depth of the observations, the observation time after the GW trigger, and the density of stars in the field.

6.2. QUEST

The QUEST pipeline's recovery efficiency was evaluated separately for each on-source galaxy region. As for TAROT and Zadko, 100 simulated transients were added to the images for each model (kilonova, short and long GRBs) and distance. Randomly distributed magnitudes between the brightest and faintest GRBs (see normalization in Table 1) were used. Figures 9–11 show some representative examples of the achieved recovery efficiencies. The wide range in the recovery efficiencies reflects variations in CCD sensitivity and rates of contaminating artifacts. In addition, bright galaxy extended emission prevented the recovery of some injections, even at close distances. A similar efficiency loss was found when a large part of the on-source region was occupied by foreground stars or image problems like bad pixels and bad lines. The results for the QUEST observations can be characterized by the mean and the standard deviation of the distances corresponding to 50% efficiency to recover injections. For trigger G20190, we found mean distances of 33 Mpc ($\sigma = 7$ Mpc) for kilonovae, 30 Mpc ($\sigma = 6$ Mpc) for short GRBs, and 820 Mpc ($\sigma \approx 180$ Mpc) for long GRBs. For G23004, a mean distance of 64 Mpc ($\sigma = 25$ Mpc) for kilonovae, 63 Mpc ($\sigma = 30$ Mpc) for short GRBs, and 1530 Mpc ($\sigma \approx 700$ Mpc) for long GRBs were found.[161] The larger spreads for

[160] The 10% of the total on-source area within the gaps between the CCDs does not have data and was not analyzed.

[161] Taking into account the galaxy regions lying in the CCD gaps, the 50% efficiency distances for G20190 (G23004) reduce to 32 (61) Mpc for kilonovae, 26 (53) Mpc for short GRBs, and 700 (1260) Mpc for long GRBs.

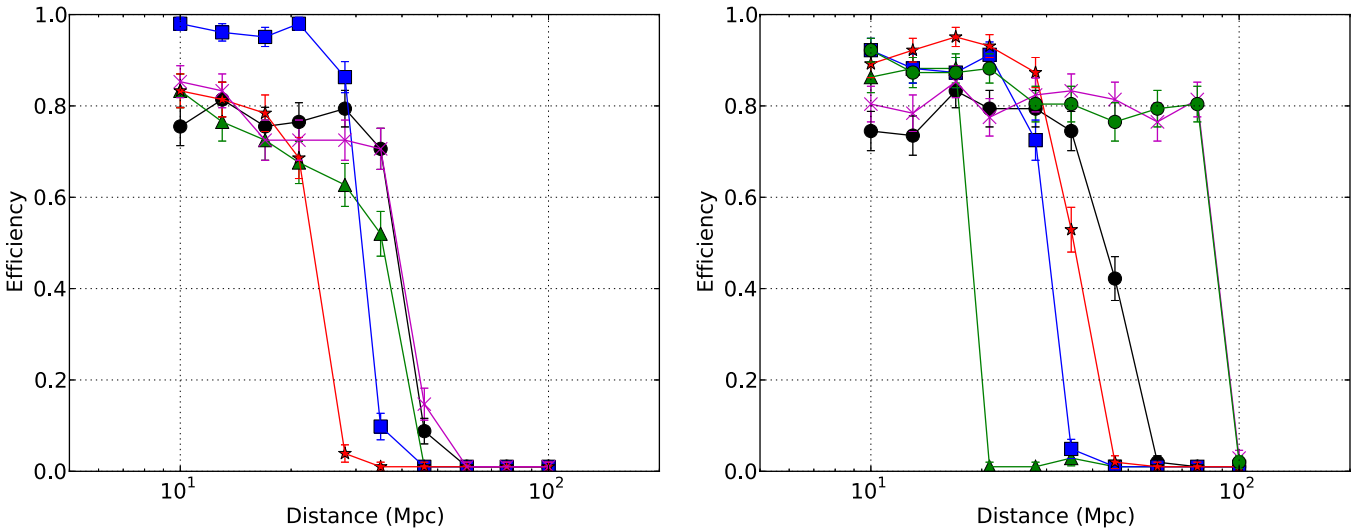

Figure 9. Some representative success rates in recovering simulated kilonovae lightcurves with the QUEST data for triggers G20190 (left) and G23004 (right). Each curve represents the efficiency from individual on-source galaxy regions, and so does not include efficiency lost due to observing only a fraction of the possible source locations.

(A color version of this figure is available in the online journal.)

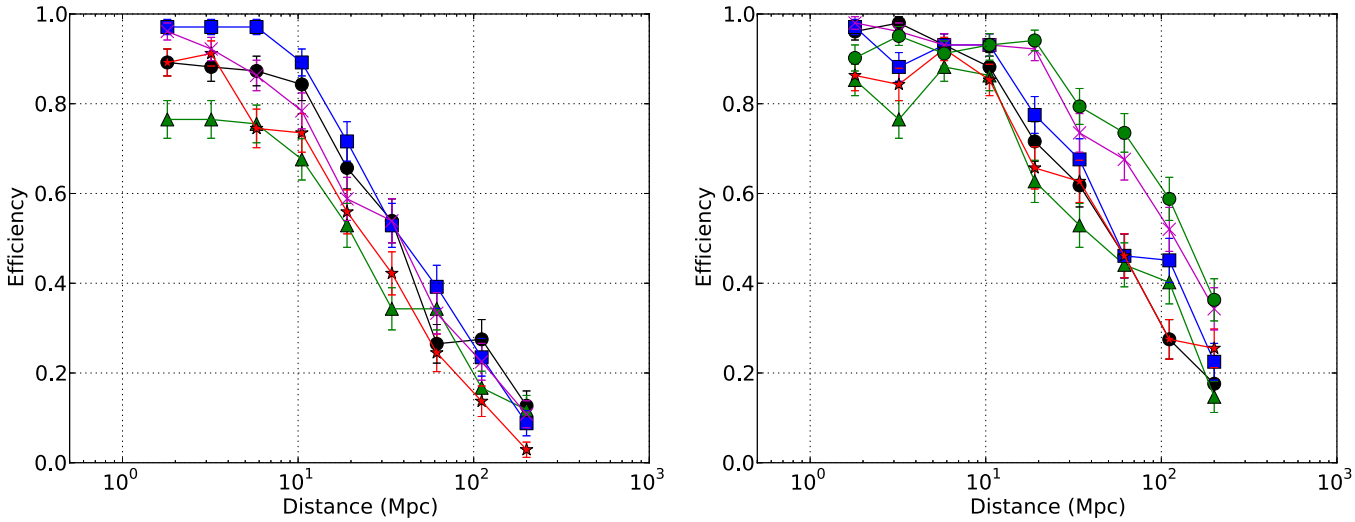

Figure 10. Some representative success rates in recovering simulated short GRB afterglow light curves with the QUEST data for triggers G20190 (left) and G23004 (right). Each curve represents the results from individual on-source galaxy regions, and so does not include efficiency lost due to observing only a fraction of the possible source locations. Each simulated afterglow lightcurve was randomly scaled within the range of normalization conditions showed in Table 1.

(A color version of this figure is available in the online journal.)

QUEST reflect CCD-to-CCD variations. For both GW triggers, the 50% efficiency distances for long GRB afterglows were well beyond the maximum distance that the LIGO and Virgo detectors could have detected signals coming from NS binary coalescences, while the kilonova and short GRB distances were comparable. However, the result obtained for the kilonova transients is dependent on the adopted model and relies on the fact that the QUEST observations were made around the peak time of the light curve model used for this study.

6.3. ROTSE

For each set of images collected by ROTSE, 140 simulated transients were added to the data for each counterpart model for 10 different distances. The PSFs for the injected transients were modeled on "good" objects PSFs within each image, as described in White et al. (2012). The GRB models used the brightest normalizations shown in Table 1; i.e., assuming magnitude 16 (23) at 1 day from $z = 1$ for LGRB (SGRB) afterglows. The results are presented in Figure 13. For each GW trigger, the efficiencies for the different counterpart models are very similar as functions of the injection magnitude. The efficiencies peak at ∼70%–80% for triggers G19377 and G20190, and at ∼55% for G21852. Trigger G23004 (not shown) contained images of very poor quality and the injection efficiency only reached a maximum of ∼20%. Long GRB afterglows/short GRB afterglows/kilonovae were recovered with 50% detection efficiency to distances of 400 Mpc/16 Mpc/2 Mpc for trigger G19377, 1000 Mpc/40 Mpc/5 Mpc for trigger G20190, and 1000 Mpc/90 Mpc/5 Mpc for trigger G21852. The maximum sensitive distances correspond to transient magnitudes of approximately 15 on the second night. This was typical of the

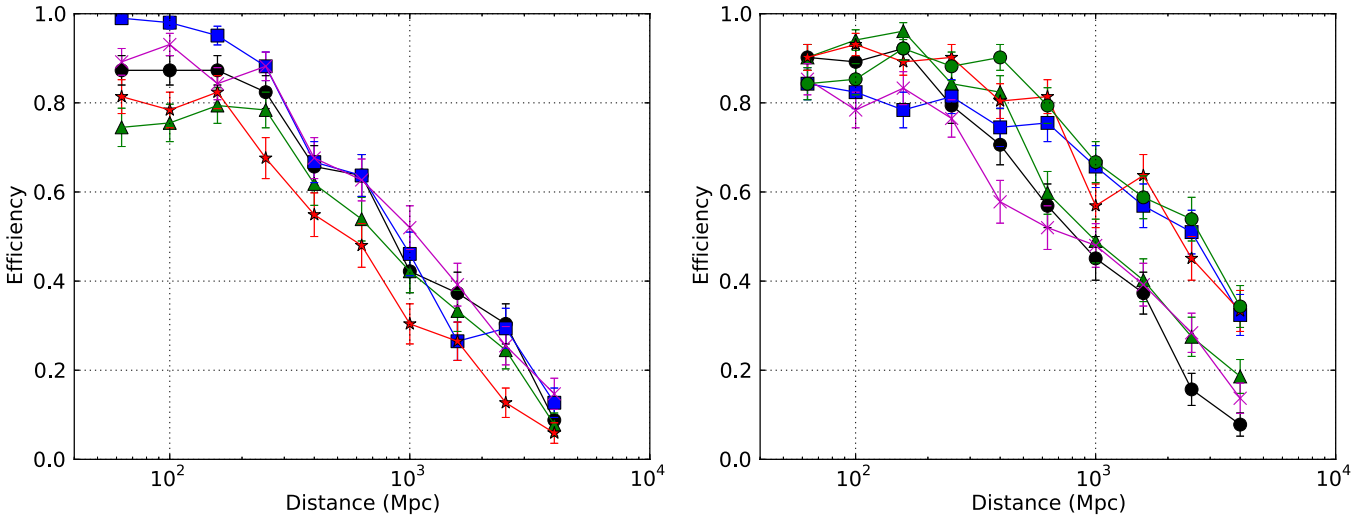

Figure 11. Some representative success rates recovering simulated long GRB light curves with the QUEST data for triggers G20190 (left) and G23004 (right). Each curve shows the results from individual on-source galaxy regions, and so does not include efficiency lost due to observing only a fraction of the possible source locations. Each simulated afterglow lightcurve was randomly scaled within the range of normalization conditions showed in Table 1.

(A color version of this figure is available in the online journal.)

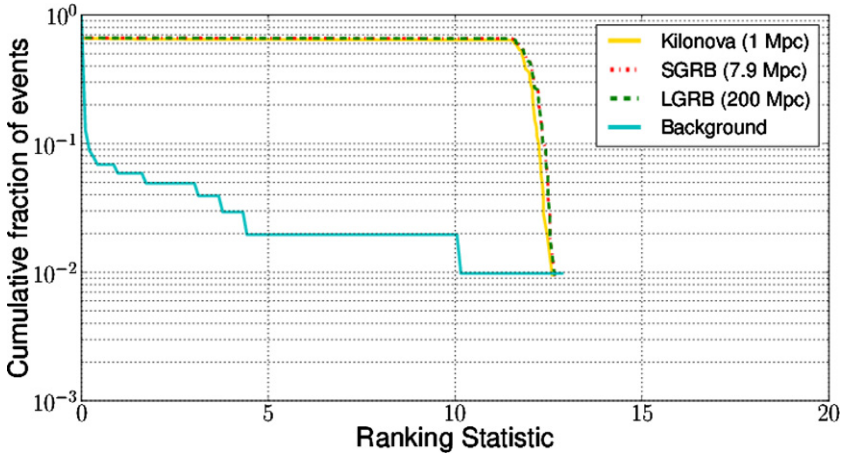

Figure 12. Distribution of ROTSE background (time-shifted) triggers and recovered injections for event G19377. This plot shows the distribution ranking statistic for kilonova injections simulated from 1 Mpc, short GRBs from 7.9 Mpc, and long GRBs from 200 Mpc. The GRB models correspond to the brightest observed GRB afterglows.

(A color version of this figure is available in the online journal.)

average limiting magnitude of ROTSE over the FOV. Since the pipeline required transients to be seen on at least two nights, the magnitude on the second night was the primary factor determining the sensitivity to each model. Transients at much smaller distances tended to suffer from saturation and were discarded in the image subtraction. The maximum detection efficiency was less than 100% because the pipeline was not always able to produce the background-subtracted lightcurve for a transient; this depended on the position in the image and on the image quality, as 16 reference stars were needed in the region around the transient for accurate image subtraction. Variations in efficiency between triggers were due mainly to differences in image quality and also differences in CCD performance between the different telescopes in the ROTSE network.

An example of the distribution of injections against the background can be seen in Figure 12. This figure shows that of all the injections that produced a nonzero ranking statistic with the specific distance scales shown, more than 60% of the injections were recovered with a rank comparable to the most highly ranked background event. However, none of the injections were found with a ranking statistic higher than loudest background event. As the injection distances increased, the injections fell more and more within the background.

6.4. Liverpool Telescope

The efficiency of the Liverpool Telescope pipeline was measured with the same methods used for ROTSE. A Python script was written to inject 100 transient objects per 10 Mpc bin per model, with light curves following the three models described in Table 1, assuming the brightest normalization for the GRB models. These images were then analyzed using the pipeline, and a script used to find and flag injections found in the pipeline output. Figure 14 shows that we obtained efficiencies around 90% for injections brighter than the limiting magnitude, including saturated objects normally discarded in other image subtraction methods. For RATCam, any of the tested models would have been observable out to 100 Mpc or more—well beyond the initial LIGO/Virgo horizon distance for NS mergers.

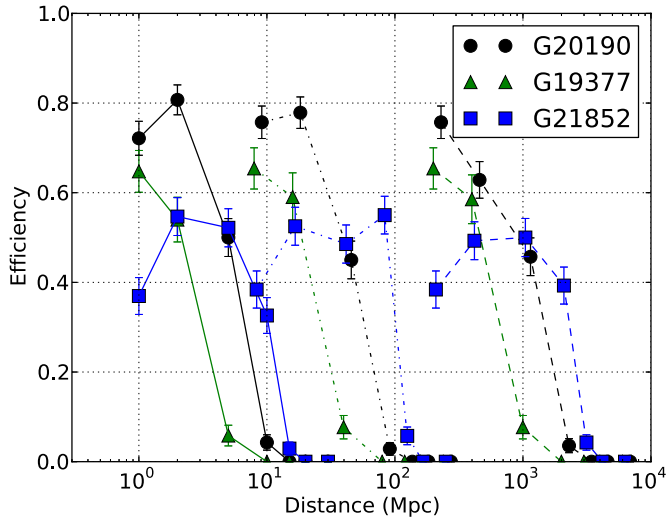

Figure 13. Efficiency of the ROTSE pipeline in recovering simulated kilonovae transients (left, solid), short GRBs (middle, dash-dotted), and long GRBs (right, dashed). The figure reflects the success rate in recovering transients added to the observed fields, and does not include efficiency lost due to observing only a fraction of the possible source locations. The efficiencies shown for the GRB afterglow models are based on the brightest models shown in Table 1. At very close distances, the simulated objects became so bright that they caused saturations in the data, and were missed by the pipeline. The images associated with trigger G23004 were of poor quality, so the efficiencies with this data are not shown.

(A color version of this figure is available in the online journal.)

For SkyCamZ, we found similar efficiencies, over smaller distance ranges.

6.5. Pi of the Sky

The efficiency of the POTS transient search was investigated by adding simulated stars to existing images and reprocessing them. The objects that were injected had different magnitudes and were chosen from real observed stars during the autumn science run. Unlike the other simulations described in this paper, objects added to POTS data did not follow model light curves, but instead measured the ability of the pipeline to recover a transient of a given magnitude using data from a single night. Stars injected in one image were also injected in subsequent images of that field taken during the same night. Only injections that were made to the inner part of the CCD chip, at least 150 pixels from CCD borders, were considered to estimate transient detection efficiency. The border part of the CCD was rejected by the off-line optical transient recognition algorithm due to the possibility of CCD anomalies that might be mistaken as short optical transients. Also, only injections starting on a good quality image were considered in efficiency estimation. This means that the effective FOV for optical transient recognition corresponds to $15^\circ \times 15^\circ$. At each stage of the processing it was determined how many of the injected objects were detected.

Figure 15 shows two curves demonstrating the efficiency of the POTS pipeline. The first one describes how many of the injected objects were detected in at least one image and the second curve shows how many of the injections were detected in five or more images. The first case corresponds to the minimal criterion that was required for the candidate to be classified as an optical transient and be inspected by a human. The second case reflects the criteria used for an optical transient to have been automatically classified as a nearly certain real event. On both curves we see that the maximal efficiency did not reach near 100%, even for very bright sources. This can be attributed to several causes. An important loss of efficiency came from areas excluded from the search due to the presence of previously discovered stars. Objects injected within a radius of $150''$ of stars listed in the POTS star catalogue were not recognized as optical transients and discarded by the pipeline, resulting in a 12%–15% impact to the injection recovery rate. Additional sources were lost to structure in the CCD: 10%–15% of the CCD area consisted of wire guiding electric charge. A significant part of the losses also came from quality checks in the algorithm preprocessing. At this stage transients that were fainter than 11th magnitude, or observed on multiple low quality frames, were discarded. This impacted the efficiency by 10% for bright transients, and up to 30% for faint transients injected with brightness around magnitude 11. Other cuts in the data processing pipeline resulted in an additional 3%–10% loss of efficiency.

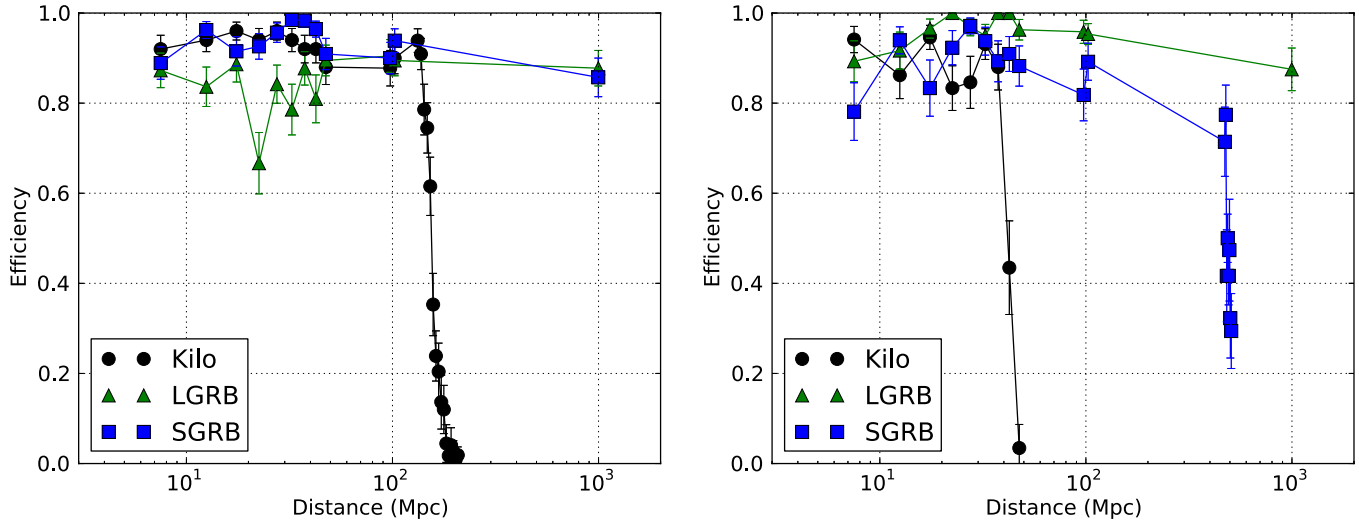

Figure 14. Success rates recovering simulated short GRB afterglows, long GRB afterglows and kilonova light curves for the Liverpool Telescope, using the RATCam (left) and SkyCamZ (right). The figure reflects the success rate in recovering transients added to the observed fields, and does not include efficiency lost due to observing only a fraction of the possible source locations. The shown results for GRB afterglows are based on the brightest models that we considered.

(A color version of this figure is available in the online journal.)

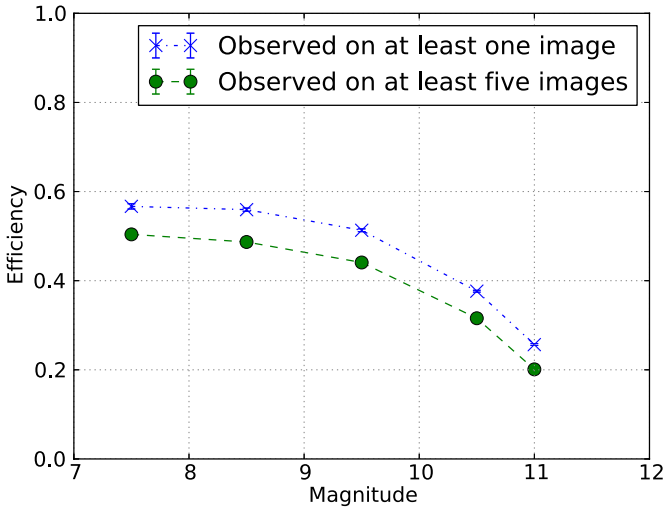

Figure 15. Success rate of the Pi of the Sky pipeline in recovering simulated transients of various magnitudes. The figure reflects the success rate in recovering transients added to the observed fields, and does not include efficiency lost due to observing only a fraction of the possible source locations. (A color version of this figure is available in the online journal.)

7. DISCUSSION AND SUMMARY

This paper describes the first end-to-end searches for optical transients associated with GW candidate events. Unfortunately, no convincing transient counterpart was found. This effort included a range of different types of telescopes, as well as a range of different analysis strategies. While the variety of analysis strategies employed presents a challenge for interpretating the results, we believe that this approach is forward-looking. The LIGO and Virgo collaborations have recently made an open call for partners to search for EM counterparts to GW events discovered with the next generation of GW detectors.[162] It is likely that partners will use a variety of facilities and instruments, and each apply their own data analysis techniques. Both the successes and lessons of this work should serve as useful guideposts to investigators pursuing similar searches with the up-coming "advanced" generation of GW detectors. Strategies are also being discussed in the literature (Metzger & Berger 2012; Nissanke et al. 2013; Singer et al. 2013).

Rapidly down-selecting candidates for follow-up observations, integrating results for astrophysical interpretation, and communicating findings will require a common framework to describe transients discovered with disparate techniques. In this work, we presented two complementary statistics for characterizing the results of a transient classification pipeline, the FAP and the detection efficiency. These statistics were calculated for several different analyses, so that objects discovered in the searches could be quantitatively evaluated and compared. This paradigm, where results from transient searches with different selection criteria must be discussed in a common language, is likely to be a theme that becomes more common as survey instruments evolve.

Because GW event candidates are poorly localized, searches for counterparts need to consider the large population of optically variable sources that could produce false positive coincidences (Kulkarni & Kasliwal 2009). Classification based on light curves, spectroscopy and other properties can help, but these strategies are complicated by the fact that the light curves associated with compact object mergers and other potential GW sources are largely uncertain. However, we were able to demonstrate several automated strategies that reduced false positives, while selecting for a wide range of models. These techniques included demands on the rate of dimming in objects, spatial coincidence with galaxies within the GW observable distance, anti-coincidence with cataloged stars and asteroids, and shapes consistent with point objects. For a variety of data sets over wide areas, we showed how these cuts could be applied to reduce the rate of false positives to less than 10%, meaning that a single telescope taking a series of images in response to a GW trigger would have less than a 10% chance of reporting a false positive. Monte Carlo simulations of model light curves were used to show that this false-positive rejection was possible while still maintaining sensitivity to models of both GRB afterglow light curves and kilonova light curves.

Follow-up observations of the type presented in this paper will probably be just the first stage in efforts to find Advanced LIGO/Virgo counterparts. While essential to identify candidate counterparts, wide field imaging is unlikely to be sufficient to make definitive associations with a GW trigger. Further observations, including sensitive photometry and spectroscopy, will be needed to confirm possible associations and characterize the source. The level of false-positive rejection achieved by software in this work, if promptly applied to collected optical image data, would reduce candidate objects associated with a LIGO/Virgo trigger to a manageable level, such that they could be pursued with further follow-up observations. The challenge presented by false positives is likely to increase with the advent of Advanced LIGO/Virgo, when a larger horizon distance will require imaging to fainter magnitudes, and so increase the number of potential contaminants.

The Monte Carlo studies we performed demonstrated that we typically recovered a range of light curve models to a depth consistent with the limiting flux of the observations, proving the validity of our selection criteria. During the observing periods, typical position averaged sensitive ranges for NS–NS mergers was 18 Mpc, or 35 Mpc for NS–BH mergers (Abadie et al. 2012e). The efficiency curves shown in Figures 9 through 15 show that the data sets with better limiting magnitudes (QUEST, Liverpool Telescope) were successful in recovering all the considered models at these distance scales. The less sensitive data sets (ROTSE, TAROT, Zadko) would have missed a kilonova at these distances, but were potentially sensitive to GRB afterglows. Looking toward the future, the simulation results show that short exposures (∼1 minute) with small aperture telescopes, with observations to depths of less than 18th magnitude, failed to recover short GRB or kilonova light curves at distances comparable to the expected 200 Mpc range of advanced GW detectors to NS–NS mergers (Abadie et al. 2010b; Aasi et al. 2013). This means that, while smaller telescopes may be valuable in searching for counterparts to galactic GW sources, they may require long total exposures, and/or a hierarchical observing strategy with larger telescopes, to be able to detect the expected optical signature of distant compact object mergers. Another factor that is likely to impact transient recovery in the advanced detector era is the incompleteness of available galaxy catalogs (Nissanke et al. 2013). Currently, catalogs are missing a significant fraction of the extragalactic starlight within 200 Mpc, however, planned surveys can help address this problem (Nissanke et al. 2013).

This study has been a valuable exercise that will help the preparation of the data analysis and observing strategies for

[162] http://www.ligo.org/science/GWEMalerts.php

the up-coming second generation GW detectors, which are anticipated to begin operating in 2015 and to improve in sensitivity over the following few years (Aasi et al. 2013). Searches for optical and other transient counterparts will become even more compelling as the range of the detectors increases. Moreover, the rapid growth of large area survey instruments, including plans for the Large Synoptic Survey Telescope (Ivezic et al. 2011), means that the problem of choosing among rapidly fading candidates selected with different criteria is likely to become a theme that extends beyond GW related searches. The LIGO and Virgo collaborations are committed to providing prompt triggers for astronomers to follow up, with a more open model to allow broader participation (LIGO Scientific Collaboration & Virgo Collaboration 2012). We can therefore hope that future searches will yield multi-messenger transient events that reveal the astrophysical sources and processes that produce them.

We thank J. Barnes, D. Kasen, B. Metzger, and E. Nakar for providing the kilonova model light curves that we have used in our Figures 4–7.

The authors gratefully acknowledge the support of the United States National Science Foundation for the construction and operation of the LIGO Laboratory, the Science and Technology Facilities Council of the United Kingdom, the Max-Planck-Society, and the State of Niedersachsen/Germany for support of the construction and operation of the GEO600 detector, and the Italian Istituto Nazionale di Fisica Nucleare and the French Centre National de la Recherche Scientifique for the construction and operation of the Virgo detector. The authors also gratefully acknowledge the support of the research by these agencies and by the Australian Research Council, the International Science Linkages program of the Commonwealth of Australia, the Council of Scientific and Industrial Research of India, the Istituto Nazionale di Fisica Nucleare of Italy, the Spanish Ministerio de Economia y Competitividad, the Conselleria d'Economia Hisenda i Innovacio of the Govern de les Illes Balears, the Foundation for Fundamental Research on Matter supported by the Netherlands Organisation for Scientific Research, the Polish Ministry of Science and Higher Education, the FOCUS Programme of Foundation for Polish Science, the Royal Society, the Scottish Funding Council, the Scottish Universities Physics Alliance, The National Aeronautics and Space Administration, OTKA of Hungary, the Lyon Institute of Origins (LIO), the National Research Foundation of Korea, Industry Canada and the Province of Ontario through the Ministry of Economic Development and Innovation, the National Science and Engineering Research Council Canada, the Carnegie Trust, the Leverhulme Trust, the David and Lucile Packard Foundation, the Research Corporation, FIRB 2012 Project RBFR12PM1F (Italian Ministry of Education, University and Research), and the Alfred P. Sloan Foundation. This work is based on results partially obtained at the ESO observatory, La Silla. The Liverpool Telescope is operated on the island of La Palma by Liverpool John Moores University in the Spanish Observatorio del Roque de los Muchachos of the Instituto de Astrofisica de Canarias with financial support from the UK Science and Technology Facilities Council. This document has been assigned the identifier LIGO-P1200171-v19.

REFERENCES

Aasi, J., Abadie, J., Abbott, B. P., et al. 2013, arXiv:1304.0670
Abadie, J., Abbott, B. P., Abbott, R., et al. 2012a, PhRvD, 85, 122007
Abadie, J., Abbott, B. P., Abbott, R., et al. 2012b, ApJ, 760, 12
Abadie, J., Abbott, B. P., Abbott, R., et al. 2012c, A&A, 541, A155
Abadie, J., Abbott, B. P., Abbott, R., et al. 2012d, A&A, 539, A124
Abadie, J., Abbott, B. P., Abbott, R., et al. 2012e, PhRvD, 85, 082002
Abadie, J., Abbott, B. P., Abbott, R., et al. 2010a, PhRvD, 81, 102001
Abadie, J., Abbott, B. P., Abbott, R., et al. 2010b, CQGra, 27, 173001
Abbott, B. P., Abbott, R., Adhikari, R., et al. 2009, RPPh, 72, 076901
Abdo, A. A., Ackermann, M., Arimoto, M., et al. 2009, Sci, 323, 1688
Accadia, T., Acernese, F., Alshourbagy, M., et al. 2012, JINST, 7, P03012
Akerlof, C. W., Kehoe, R. L., McKay, T. A., et al. 2003, PASP, 115, 132
Alard, C. 2000, A&AS, 144, 363
Alard, C., & Lupton, R. 1998, ApJ, 503, 325
Baltay, C., Rabinowitz, D., Andrews, P., et al. 2007, PASP, 119, 1278
Barnes, J., & Kasen, D. 2013, ApJ, 775, 18
Beauville, F., Bizouard, M.-A., Blackburn, L., et al. 2008, CQGra, 25, 045001
Berger, E. 2010, ApJ, 722, 1946
Berger, E., Fong, W., & Chornock, R. 2013, ApJL, 774, L23
Bertin, E., & Arnouts, S. 1996, A&AS, 117, 393
Bloom, J. S., Richards, J. W., Nugent, P. E., et al. 2012, PASP, 124, 1175
Brink, H., Richards, J. W., Poznanski, D., et al. 2013, MNRAS, 435, 1047
Cavalier, F., Barsuglia, M., Bizouard, M.-A., et al. 2004, PhRvD, 74, 082004
Clocchiatti, A., Suntzeff, N. B., Covarrubias, R., & Candia, P. 2011, AJ, 141, 163
Corsi, A., & Mészáros, P. 2009, ApJ, 702, 1171
Costa, E., Frontera, F., Heise, J., et al. 1997, Natur, 387, 783
Coward, D. M., Todd, M., Vaalsta, T. P., et al. 2010, PASA, 27, 331
Davies, M. B., King, A., Rosswog, S., & Wynn, G. 2002, ApJL, 579, L63
Doggett, J. B., & Branch, D. 1985, AJ, 90, 2303
Droege, T. F., Richmond, M. W., Sallman, M. P., & Creager, R. P. 2006, PASP, 118, 1666
Eichler, D., Livio, M., Piran, T., & Schramm, D. N. 1989, Natur, 340, 126
Evans, P. A., Fridriksson, J. K., Gehrels, N., et al. 2012, ApJS, 203, 28
Faber, J. A., & Rasio, F. A. 2012, LRR, 15, 8
Fairhurst, S. 2011, CQGra, 28, 105021
Fong, W., Berger, E., Margutti, R., et al. 2012, ApJ, 756, 189
Frail, D. A., Kulkarni, S. R., Nicastro, L., Feroci, M., & Taylor, G. B. 1997, Natur, 389, 261
Frail, D. A., Kulkarni, S. R., Sari, R., et al. 2001, ApJL, 562, L55
Fryer, C. L., Holz, D. E., & Hughes, S. A. 2002, ApJ, 565, 430
Gal-Yam, A., Kasliwal, M. M., Arcavi, I., et al. 2011, ApJ, 736, 159
Galama, T. J., Vreeswijk, P. M., van Paradijs, J., et al. 1998, Natur, 395, 670
Gehrels, N., Cannizzo, J. K., & Norris, J. P. 2007, NJPh, 9, 37
Gehrels, N., Sarazin, C. L., O'Brien, P. T., et al. 2005, Natur, 437, 851
Granot, J., Panaitescu, A., Kumar, P., & Woosley, S. E. 2002, ApJL, 570, L61
Grote, H., & LIGO Scientific Collaboration, 2008, CQGra, 25, 114043
Harrison, F. A., Bloom, J. S., Frail, D. A., et al. 1999, ApJL, 523, L121
Harry, G. M., & LIGO Scientific Collaboration 2010, CQGra, 27, 084006
Hjorth, J., Watson, D., Fynbo, J. P. U., et al. 2005, Natur, 437, 859
Ivezic, Z., Tyson, J. A., Acosta, E., et al. 2011, LSST: From Science Drivers to Reference Design and Anticipated Data Products (arXiv:0805.2366v2)
Jenkner, H., Lasker, B. M., Sturch, C. R., et al. 1990, AJ, 99, 2082
Kann, D. A., Klose, S., Zhang, B., et al. 2010, ApJ, 720, 1513
Kann, D. A., Klose, S., Zhang, B., et al. 2011, ApJ, 734, 96
Kanner, J., Huard, T. L., Marka, S., et al. 2008, CQGra, 25, 184034
Keller, S. C., Schmidt, B. P., Bessell, M. S., et al. 2007, PASA, 24, 1
Klimenko, S., Vedovato, G., Drago, M., et al. 2011, PhRvD, 83, 102001
Klotz, A., Boer, M., Atteia, J. L., & Gendre, B. 2009, AJ, 137, 4100
Kobayashi, S., & Mészáros, P. 2003, ApJ, 589, 861
Kochanek, C. S., & Piran, T. 1993, ApJL, 417, L17
Kouveliotou, C., Meegan, C. A., Fishman, G. J., et al. 1993, ApJL, 413, L101
Kulkarni, S. R., & Kasliwal, M. M. 2009, Astrophysics with All-Sky X-Ray Observations (Saitama: RIKEN, and JAXA Suzuki Umetaro Hall, RIKEN Wako), 312
Law, N. M., Kulkarni, S. R., Dekany, R. G., et al. 2009, PASP, 121, 1395
Lazio, J., Keating, K., Jenet, F. A., et al. 2012, in IAU Symp. 285, New Horizons in Time-Domain Astronomy, ed. R. E. M. Griffin, R. J. Hanisch, & R. Seaman (Cambridge: Cambridge Univ. Press), 67
Li, L., & Paczyński, B. 1998, ApJL, 507, L59
LIGO Scientific Collaboration, & Virgo Collaboration 2012, LIGO DCC, M1200055, https://dcc.ligo.org/LIGO-M1200055-v2/public
MacFadyen, A. I., & Woosley, S. E. 1999, ApJ, 524, 262
Malek, K., Batsch, T., Cwiok, M., et al. 2009, Proc. SPIE, 7502, 75020D
Mészáros, P. 2006, RPPh, 69, 2259
Metzger, B. D., & Berger, E. 2012, ApJ, 746, 48
Metzger, B. D., Martínez-Pinedo, G., Darbha, S., et al. 2010, MNRAS, 406, 2650
Molinari, E., Vergani, S. D., Malesani, D., et al. 2007, A&A, 469, L13

Monet, D., Bird, A., Canzian, B., Dahn, C., et al. 1998, The USNO-A2.0 Catalogue (Washington, DC: U.S. Naval Observatory)
Nakar, E. 2007, PhR, 442, 166
Narayan, R., Paczynski, B., & Piran, T. 1992, ApJL, 395, L83
Nissanke, S., Kasliwal, M., & Georgieva, A. 2013, ApJ, 767, 124
Nissanke, S., Sievers, J., Dalal, N., & Holz, D. 2011, ApJ, 739, 99
Nousek, J. A., Kouveliotou, C., Grupe, D., et al. 2006, ApJ, 642, 389
Nuttall, L. K., & Sutton, P. J. 2010, PhRvD, 82, 102002
Nuttall, L. K., White, D. J., Sutton, P. J., et al. 2013, ApJS, 209, 24
Ott, C. D. 2009, CQGra, 26, 063001
Paczynski, B. 1991, AcA, 41, 257
Piran, T., Nakar, E., & Rosswog, S. 2013, MNRAS, 430, 2121
Piro, A. L., & Pfahl, E. 2007, ApJ, 658, 1173
Racusin, J. L., Liang, E. W., Burrows, D. N., et al. 2009, ApJ, 698, 43
Racusin, J. L., Oates, S. R., Schady, P., et al. 2011, ApJ, 738, 138
Rahmer, G., Smith, R., Velur, V., et al. 2008, Proc. SPIE, 7014, 70144Y
Rau, A., Kulkarni, S. R., Law, N. M., et al. 2009, PASP, 121, 1334
Rhoads, J. E. 2003, ApJ, 591, 1097
Roberts, L. F., Kasen, D., Lee, W. H., & Ramirez-Ruiz, E. 2011, ApJL, 736, L21
Romero, G. E., Reynoso, M. M., & Christiansen, H. R. 2010, A&A, 524, A4
Sari, R., Piran, T., & Halpern, J. P. 1999, ApJL, 519, L17
Sari, R., Piran, T., & Narayan, R. 1998, ApJL, 497, L17
Searle, A. C., Sutton, P. J., Tinto, M., & Woan, G. 2008, CQGra, 25, 114038
Shibata, M., Karino, S., & Eriguchi, Y. 2003, MNRAS, 343, 619
Shibata, M., & Taniguchi, K. 2011, LRR, 14, 6
Singer, L. P., Cenko, S. B., Kasliwal, M. M., et al. 2013, ApJL, 776, L34
Smith, A. M., Lynn, S., Sullivan, M., et al. 2011, MNRAS, 412, 1309
Soderberg, A. M., Nakar, E., Berger, E., & Kulkarni, S. R. 2006, ApJ, 638, 930
Sokolowski, M. 2008, PhD thesis, Andrzej Soltan Institute for Nuclear Studies (arXiv:0810.1179)
Steele, I. A., Smith, R. J., Rees, P. C., et al. 2004, Proc. SPIE, 5489, 679
Tanvir, N. R., Levan, A. J., Fruchter, A. S., et al. 2013, Natur, 500, 547
Thorne, K. S. 1987, in Gravitational Radiation, ed. S. W. Hawking & W. Israel (Cambridge: Cambridge Univ. Press), 330
van Eerten, H., Zhang, W., & MacFadyen, A. 2010, ApJ, 722, 235
van Eerten, H. J., & MacFadyen, A. I. 2011, ApJL, 733, L37
van Paradijs, J., Groot, P. J., Galama, T., et al. 1997, Natur, 386, 686
Virgo Collaboration 2009, Advanced Virgo Baseline Design, Tech. Rep., VIR-0027A-09, https://tds.ego-gw.it/ql/?c=6589
Vitale, S., Del Pozzo, W., Li, T. G. F., et al. 2012, PhRvD, 85, 064034
White, D. J., Daw, E. J., & Dhillon, V. S. 2011, CQGra, 28, 085016
White, D. J., LIGO Scientific Collaboration, & Virgo Collaboration 2012, JPhCS, 363, 012036
Woosley, S. E. 1993, ApJ, 405, 273
Woosley, S. E., & Bloom, J. S. 2006, ARA&A, 44, 507
Yuan, F., & Akerlof, C. W. 2008, ApJ, 677, 808